Fabrication and characterization of micrometer-thin, color center-enriched diamonds for open microcavity quantum network nodes

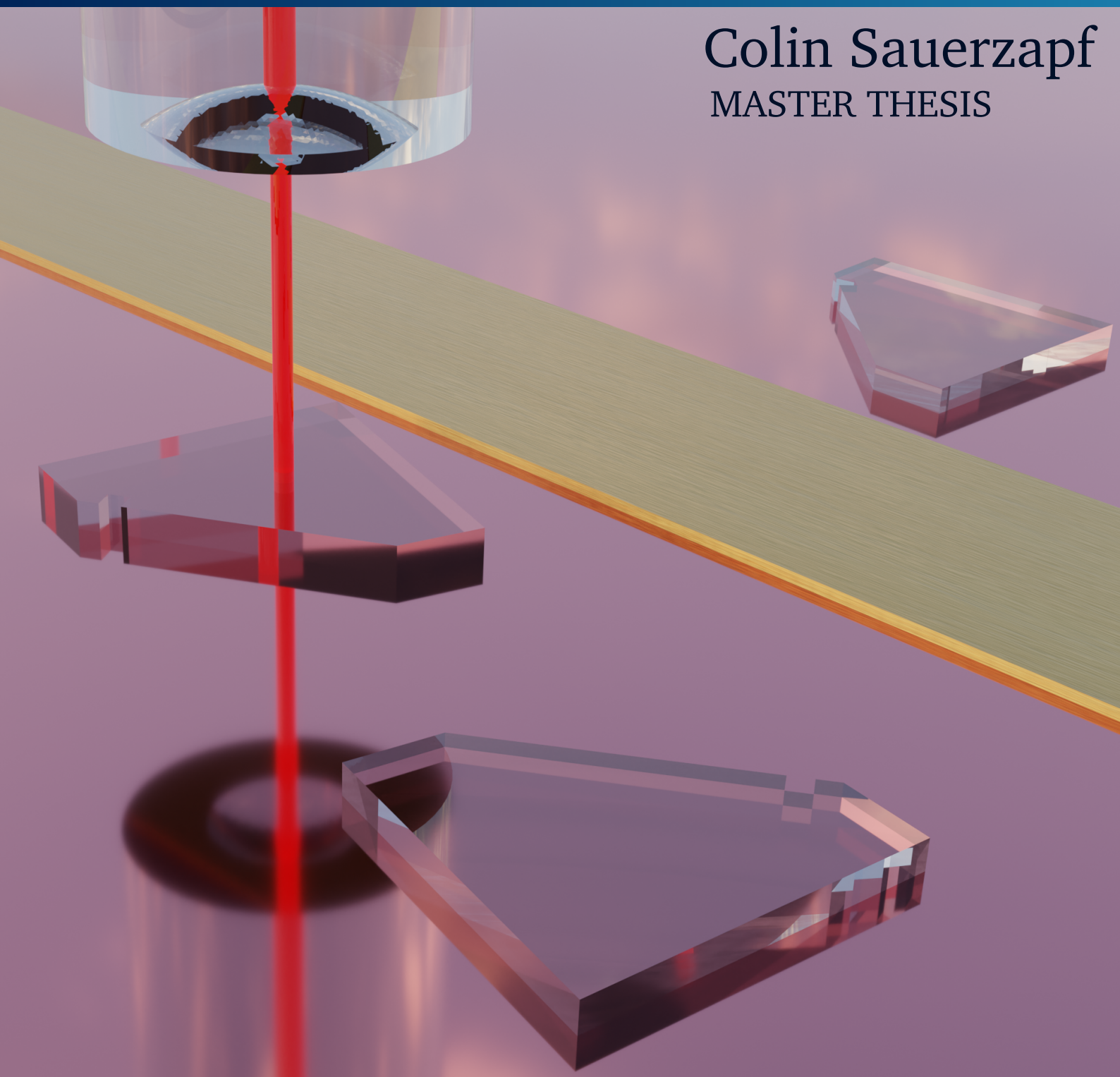

Colin Sauerzapf

MASTER THESIS

Thesis Committee: Prof. Jörg Wrachtrup
Prof. Tilman Pfau

Supervisors: Prof. Jörg Wrachtrup
Prof. Ronald Hanson

Daily Supervisors: Julia Brevoord
Julius Fischer

2023

Erklärung der Selbstständigkeit

Hiermit versichre ich gemäß der Prüfungsordnung vom 31.07.2015 des Studiengangs Physik Master of Science,

- dass ich die Arbeit selbstständig verfasst habe,
- dass ich keine anderen als die angegebenen Quellen benutz und alle wörtlichen oder sinngemäßen aus anderen Werken übernommenen Aussagen als solche gekennzeichnet habe,
- dass die eingereichte Arbeit weder vollständig noch in wesentlichen Teilen Gegenstand eines anderen Prüfungsverfahrens gewesen ist, und
- dass das elektronische Exemplar mit den anderen Exemplaren übereinstimmt.

Colin Sauerzapf

ZUSAMMENFASSUNG

Das Stickstoff-Fehlstellen-Zentrum (NV) in Diamant kann als Quantennetzwerkknoten genutzt werden [1, 2], allerdings limitiert der niedrige Debye-Waller-Faktor $\beta_0 \approx 3\,\%$ [3, 4] die Verschränkungsrate des Systems drastisch. Durch die Einbettung des Farbzentrums in eine offene Fabry-Pérot Mikrokavität und die Ausnutzung des Purcell-Effekts kann diese Einschränkung verringert werden [3, 5]. Da die Kopplung eines Emitters an einen optischen Resonator auch die Sammeleffizienz der emittierten kohärenten Photonen erhöht, ist ein solches System auch für Emitter mit einem höheren intrinsischen Debye-Waller-Faktor interessant, wie zum Beispiel dem Zinn-Fehlstellen-Zentrum (SnV) in Diamant. Ein wichtiger Baustein eines solchen Resonantors ist die Diamantprobe, die sich zwischen den beiden Spiegeln befindet. In dieser Arbeit wird die Herstellung von einstellig mikrometerdünnen, mit Farbzentren angereicherten Diamantplättchen mit Seitenlängen von einigen zehn Mikrometern untersucht und ihre Eigenschaften nach dem Anhaften auf einen Bragg-Spiegel charakterisiert. Es wurden Plättchen mit NV-Zentren und Plättchen mit implantierten SnV-Zentren hergestellt. Neben der Herstellung mittels Elektronenstrahllithografie und Trockenätzen wir auch eine neue Methode vorgestellt, die Laserschneiden nutzt. Mit beiden Herstellungsmethoden wurde eine angemessene Anhaftungsausbeute für Plättchen erzielt und eine minimale Oberflächenrauheit von $R_q \approx 0.2\,\mathrm{nm}$ gemessen. Die Proben wurden in einem konfokalen Mikroskopieaufbau bei kryogenen Temperatur untersucht, um die optische Linienbreite der Null-Phonon-Linien Emission der Farbzentren zu bestimmen. Für die SnV-Zentren in den Diamantplättchen wurde eine annähernd lebensdauerbegrenzte [6] Dephasierungs-Linienbreite von $\Gamma_d \approx 32.2(4)\,\mathrm{MHz}$ und eine minimale spektrale Diffusionslinienbreite von $\Gamma_s \approx 58(2)\,\mathrm{MHz}$ gemessen. Für das NV-Zentrum konnte nur die spektrale Diffusionslinienbreite $\Gamma_s < 80\,\mathrm{MHz}$ gemessen werden. Diese gemessenen Linienbreiten sind schmal genug, um Quanteninterferenz durch zwei von Farbzentren emittierte Photonen zu erzeugen [7]. Zusätzlich wurden die Diamantplättchen in einem offenen Fabry-Pérot Mikrokavitätsaufbau untersucht. Mit einer durch Lithographie und Trockenätzung hergestellten, mit NV-Zentren angereicherten Probe wurde eine maximale Finesse von $\mathscr{F} \approx 3100(300)$ gemessen. Zusätzliche Verluste durch den Diamanten von $\mathscr{L}_{\mathrm{add,dia}} \approx 1200(200)\,\mathrm{ppm}$ konnten abgeschätzt werden. Für eine lasergeschnittene, mit SnV-Zentrum angereicherte Probe konnte eine maximale Finesse von $\mathscr{F} \approx 2300(200)$ erreicht werden. Unter Verwendung der Finesse und der gemessenen Resonatorparametern wurde eine Abschätzung für den maximal erreichbaren Purcell-Faktor und das daraus resultierende Verzweigungsverhältnis in die Resonatormode berechnet. Für das SnV-Zentrum wurde ein maximal erreichbarer Purcell-Faktor von $F_P^{\mathrm{ZPL}} \approx 15(2)$ berechnet, was zu einem Verzweigungsverhältnis in die Resonatormode von $\beta_{\mathrm{cav}} \approx 85(2)\,\%$ führt. Darüber hinaus wurde eine Obergrenze für den Auskopplungsprozentsatz durch den Planspiegel von $\beta_{\mathrm{out}} < 62(13)\,\%$ abgeschätzt. Für die NV-Zentrum Probe wurden $F_P^{\mathrm{ZPL}} \approx 19(2)$, $\beta_{\mathrm{cav}} \approx 37(2)\,\%$, und $\beta_{\mathrm{out}} \approx 13(6)\,\%$ bestimmt.

Abstract

The nitrogen-vacancy (NV) center in diamond can be used as a quantum network node [1], but the low Debye-Waller factor $\beta_0 \approx 3\,\%$ [3, 4] limits the entanglement rate of the system drastically. By embedding the color center into an open microcavity and utilizing the Purcell effect, this limitation can be reduced [3, 5]. Additionally, as coupling an emitter to an optical cavity enhances the collection efficiency of the emitted coherent photons, such a system is also interesting for emitters with a higher intrinsic Debye-Waller factor, as, for example, the tin-vacancy (SnV) center in diamond. The diamond sample between the cavity mirrors is an important building block of such a cavity system. In this thesis, the fabrication of single-digit micrometer-thin, color center-enriched diamond platelets with side lengths of tens of micrometers is studied. Additionally, their properties were characterized after bonding them to a Bragg mirror. Platelets containing NV centers and platelets with implanted SnV centers were produced. In addition to fabrication with electron beam (e-beam) lithography and dry etching, a new method is introduce utilizing laser cutting. A reasonable bonding yield was achieved for platelets from both fabrication methods, and a minimal surface roughness of $R_q \approx 0.2\,\text{nm}$ was measured. The samples were studied in a low-temperature confocal microscopy setup to determine the color center's optical linewidth of the zero-phonon line (ZPL) emission. For the SnV centers in the diamond platelets a close to lifetime-limited [6] dephasing linewidth of $\Gamma_d \approx 32.2(4)\,\text{MHz}$ and a minimum spectral diffusion linewidth of $\Gamma_s \approx 58(2)\,\text{MHz}$ was observed. For the NV center, only the spectral diffusion linewidth could be measured $\Gamma_s < 80\,\text{MHz}$. Those measured linewidth lay within the bounds to achieve two-photon quantum interference of separate color centers [7]. Additionally, the diamond platelets were studied in an open microcavity setup. With an e-beam-lithography and dry etching fabricated, NV center-enriched sample, a maximum finesse of $\mathscr{F} \approx 3100(300)$ was measured. Additional losses introduced by the diamond of $\mathscr{L}_{\text{add,dia}} \approx 1200(200)\,\text{ppm}$ could be estimated. For a laser cut fabricated, SnV center-enriched sample, a maximum finesse of $\mathscr{F} \approx 2300(200)$ could be achieved. An estimation for the maximum achievable Purcell enhancement and resulting branching ratio into the cavity mode was calculated using the measured finesse and cavity parameters. For the SnV center, a maximum achievable Purcell factor of $F_P^{\text{ZPL}} \approx 15(2)$ was computed, resulting in a branching ratio into the cavity mode of $\beta_{\text{cav}} \approx 85(2)\,\%$. In addition, an upper limit for the outcoupling percentage trough the plane mirror of $\beta_{\text{out}} < 62(13)\,\%$ was estimated. For the NV center sample, $F_P^{\text{ZPL}} \approx 19(2)$, $\beta_{\text{cav}} \approx 37(2)\,\%$, and $\beta_{\text{out}} \approx 13(6)\,\%$ were calculated.

Contents

Acronyms

AFM atomic force microscope. 16, 21, 23, 25, 26

ALD atomic layer deposition. 23

AOM acousto-optic modulator. 27, 28, 36, 37

APD avalanche photodiode. 28–30, 36

BS beam splitter. 27, 28, 36

CVD chemical vapor deposition. 15, 16

e-beam electron beam. iii, 15, 18–24, 33, 34, 38, 40, 43, 51, 52

EOM electro-optic modulator. 36–39

FSR free spectral range. 8, 12, 13, 37–39

FWHM full width at half maximum. 8, 12, 30, 38

ICP inductively coupled plasma. 19, 52, 53

IPA isopropyl alcohol. 19, 52–54

LF low frequency. 51

LP longpass. 28, 36

MO molecular orbitals. 3

MWG microwave generator. 28, 30

ND neutral density. 28

NV nitrogen-vacancy. iii, 1–6, 9, 10, 16, 17, 20, 22–24, 27, 28, 30–35, 38–41, 43, 44

ODMR optically detected magnetic resonance. 30, 33, 34, 44

PCB printed circuit board. 28

PD photodiode. 37–39

PECVD plasma-enhanced chemical vapor deposition. 19, 51

PID proportional–integral–derivative. 27, 29

PLE photoluminescence excitation. 28–33

PMMA poly(methyl methacrylate). 19

PSB phonon sideband. 4, 6, 9, 27

PVA poly(vinyl alcohol). 20, 21

RF radio frequency. 51–53

RIE reactive ion etching. 19

RMS root mean square. 16, 25, 26, 40

ROC rate of curvature. 14

SEM scanning electron microscope. 20–22

SnV tin-vacancy. iii, 1, 2, 5, 6, 10, 17, 20, 27–32, 34, 35, 38, 39, 41, 43, 44

SP shortpass. 28, 36

SRIM the stopping and range of ions in matter. 17

WLI white light interferometer. 23–25, 30

ZPL zero-phonon line. iii, 1, 2, 4, 6, 9, 23, 35, 38, 40, 41, 44

1 Introduction

Quantum mechanics is one of the most consequential theories in physics of the 20th century. Without it, modern computers and the internet are hard to imagine [8]. Although quantum phenomena are essential for classical computers and computer networks, the counter-intuitive consequences of quantum mechanics, such as entanglement and superposition, are not used directly [9]. It was shown that exploiting these quantum mechanical behaviors could lead to for example, faster algorithms using quantum computers [10] and secure communication using quantum networks [11]. This thesis will focus on the latter.

The key idea of a quantum internet is the ability to transfer quantum bits, or qubits, over large distances. This opens up new applications, such as secure distributed quantum computing [12] or more accurate clock synchronization [13]. Quantum network nodes are an essential building block to realize such a quantum internet [14].

A promising candidate for such a node is the nitrogen-vacancy (NV) center in diamond. The electron spin of this point defect can be used as a local qubit, which can be manipulated using microwaves [15]. Additionally, the NV center possesses an optical interface, allowing for entanglement between the electron spin and an emitted photon, which can be read out [16] or interfered with another emitted photon from a second NV to create entanglement between the two NV center's electron spins [17]. The two photons emitted by the NV centers need to be indistinguishable to achieve the entanglement. Therefore, only photons from the zero-phonon line (ZPL) (see Section 2.1.1) can be used, which for the NV center is only $\beta_0 \approx 3\,\%$ of the total emission [3, 4]. This limits the performance of the NV center as a quantum network node and makes it extremely hard to scale it up in a quantum network.

Embedding the NV center into an optical cavity and taking advantage of the Purcell effect can be a way of reducing this limitation of the NV center in diamond [3, 5]. Because the NV center is sensitive to charge noise introduced by surface charge fluctuations, embedding the color center into a nanophotonic crystal cavity and preserving the good optical properties could not be achieved as of today. A different approach, and the one studied in this thesis, is to embed the NV center-enriched diamond into a microscopic Fabry-Pérot cavity. Here, the NV center can be positioned in the order of a micrometer away from the surface, which was shown to be enough to conserve the optical properties of the color center [18] (Section 4.2.2). Coupling any emitter to such a cavity can also enhance the collection efficiency of emitted photons, making such a system also interesting for emitters with an already high intrinsic branching ratio into the ZPL, for example, the tin-vacancy (SnV) center in diamond.

One challenging aspect of integrating such a system is the fabrication of suitable, single-digit micrometer-thin diamond samples, which are bonded to one of the mirrors of the open microcavity. In this thesis, color center-enriched diamond platelet with tens of micrometers

side lengths are fabricated, bonded to a Bragg mirror, and characterized.

1.1 OUTLINE OF THE THESIS

In Chapter 2, a brief theoretical background of the NV and SnV centers in diamond is outlined. Afterward, an introduction to the Purcell enhancement of the color centers ZPL inside an optical cavity is given, and the relevant equations describing a plane-concave microcavity setup are introduced. Subsequently, the fabrication techniques for creating single-digit micrometer-thin, color center-enriched diamond platelets bonded to a mirror are shown in Chapter 3. In Chapter 4, the performed characterization measurements of the emitter properties in the fabricated diamond platelets are outlined, and the results are discussed. Additionally, the samples were studied in an open microcavity setup, for which the methods and measurement results are presented in Chapter 5. Finally, a conclusion and outlook are given in Chapter 6.

2 | THEORY

2.1 COLOR CENTERS IN DIAMOND

A diverse array of systems are studied for potential implementation as quantum network nodes, including color centers in silicon carbide [19] and rare earth ions doped in crystals [20]. Other promising systems are color centers in diamond, which are studied in this thesis.

2.1.1 THE NITROGEN-VACANCY CENTER

A multitude of defects in diamond are known. The nitrogen-vacancy (NV) center is one of the most studied color centers of them. It consists of an nitrogen (N) atom and an adjacent vacancy (V) in the diamond's carbon (C) lattice (Fig. 2.1.1 a)). The electronic wave function of the neutral state NV^0 is created by 5 electrons: 2 from the nitrogen atom and 3 more from the dangling bonds. If the NV center acquires another electron from its environment, it transforms into the NV^- state, which is the state focused on in this thesis and always meant, if not stated otherwise.

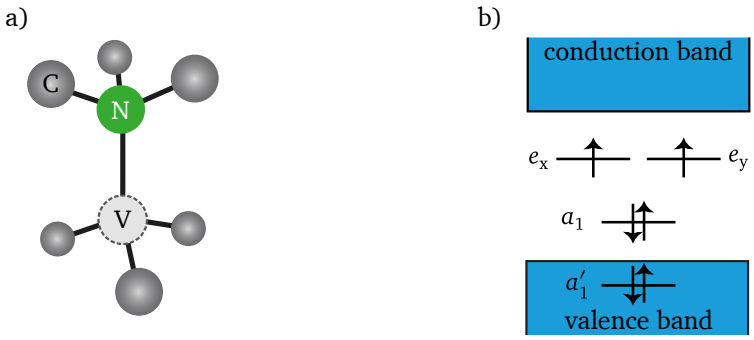

Figure 2.1.1: Adapted from Bernien, Pfaff and Ruf [7, 21, 22]. **a)** Atomic structure of the NV center in the carbon lattice. The nitrogen (N) atom is marked in green, the vacant lattice site (V) in a light gray, and the carbon (C) atoms in dark gray. **b)** Electron occupation of the NV^- ground state. The unoccupied levels in the band gap are responsible for the atomlike characteristics of the color center.

As shown in Fig. 2.1.1 b), the level structure can be expressed similarly to molecular orbitals (MO). The atomlike behavior of the NV^- can therefore be explained by the fact that the unoccupied levels of the ground state and the first optically excited state lie all inside the band gap of the diamond.

Spin-spin, spin-orbit, and Coulomb repulsion between the 6 electrons of the NV^- lead to the state structure shown in Fig. 2.1.2 b). The energetic splitting between the triplet ground state $^3A_2$ and the excited state ^3E amounts to $\Delta E_{g\to e} \approx 1.945\,\text{eV}$ or $\Delta\lambda_{g\to e} \approx 637\,\text{nm}$ (see Fig. 2.1.2 a))[23]. Decay from the excited state to the ground state is possible through the

singlet levels in between the triplet states, with the emission of an infrared photon (see Fig. 2.1.2 b)). By decay through the singlet state, a spin flip can occur [7, 24].

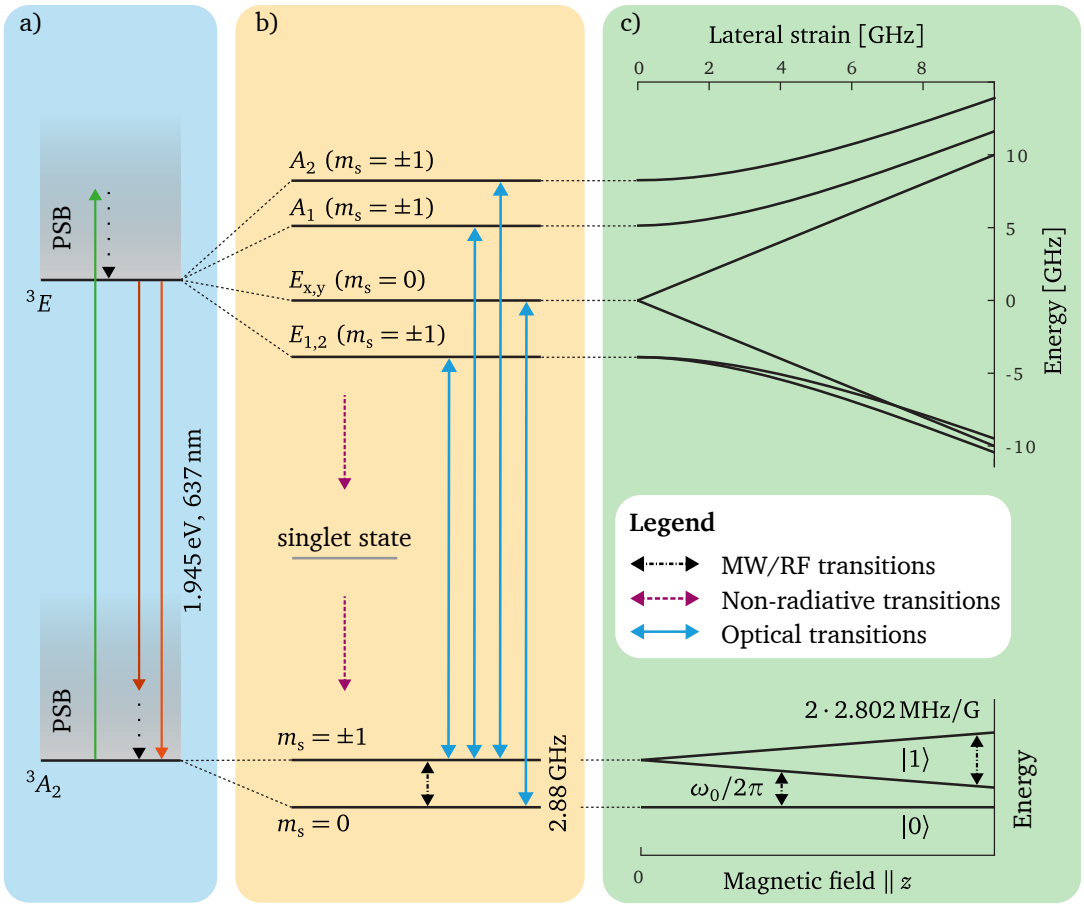

Figure 2.1.2: Electronic structure of the NV^- center adapted from Bernien and Pfaff [21, 22]. **a)** (*blue*) displays the ground state $^3A_2$ and excited state ^3E with the respective phonon sideband (PSB). **b)** (*yellow*) shows the state splitting due to spin-spin and spin-orbital interaction. These lines can only be resolved in spectroscopy at cryogenic temperatures. The blue arrows indicate optically allowed transitions (spin conserving), while the purple dotted arrows indicate non-radiative transitions. In **c)** (*green*), the level splitting of the ^3E states with perpendicular strain and the Zeeman splitting of the $m_s = \pm 1$ level of the $^3A_2$ ground state is shown. z refers here to the NV axis.

The NV center can be excited resonantly or off-resonantly, whereas, in the latter, light of higher energy or shorter wavelength is used. While in the first case, the NV is directly excited into the ^3E state, in the second case, the NV is first excited into a level of the PSB and then rapidly decaying into the ^3E state by emitting phonons. The excited state can decay into the $^3A_2$ ground state by emitting a single photon or by additionally emitting or absorbing phonons. As the phonon process adds or subtracts energy from the emitted photon, spectrally, it can be distinguished between the so-called zero phonon line zero-phonon line (ZPL) and the PSB. The ratio between the ZPL emission and the PSB emission is called Debye-Waller factor and was measured for the NV to be $\beta_0 \approx 3\,\%$ [3, 4]. Only photons from the ZPL are useful for entanglement-based quantum communication, making the low emission rate into the ZPL a disadvantage of the NV for such applications [17].

THE NV CENTER AS A QUANTUM NETWORK NODE

The NV center possesses key properties which enable it to be used as a quantum network node. The electron spin of the NV center can be used as a local qubit. Initialization into

the $m_s = 0$ (ground) state is thereby possible by off-resonant excitation and resonant spin pumping [24], while microwave driving of the ground state transitions allows for control over the spin state [7, 25]. By resonant excitation, the high cyclicity of the $m_s = 0$ transitions can be utilized for high fidelity read out, as the spin-flip probability per optical excitation is only in $\approx 0.5\,\%$ [1, 26].

2.1.2 THE YIN-VACANCY CENTER

Another color center in diamond with similar qualities as the NV center is the tin-vacancy (SnV). The color center consists of a tin atom located in an interstitial position between two vacancies of the carbon lattice. This results in a D_{3d} inversion symmetry, resulting in the absence of a permanent electric dipole. This makes it, by comparing it to the NV center, more robust against electric field fluctuation, which can especially occur due to surface charges. Therefore, the SnV center can be implemented into nanophotonic structures while preserving narrow-linewidth optical emissions [2].

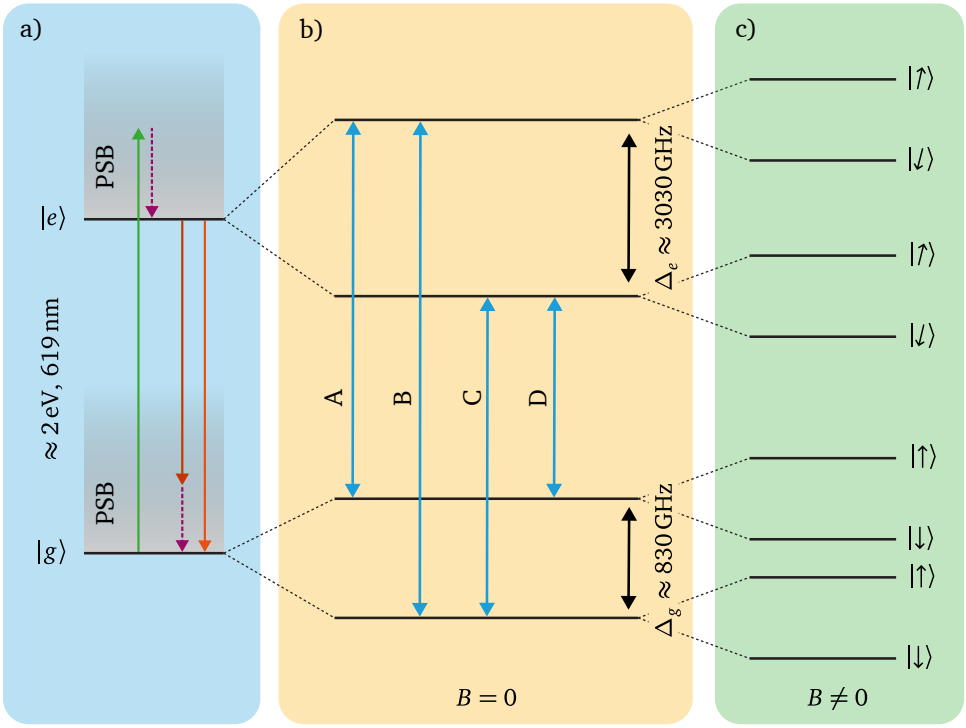

Figure 2.1.3: Electronic structure of the SnV^- center. **a)** (*blue*) displays the ground state and excited state with the respective phonon sideband (PSB). **b)** (*yellow*) shows the state splitting at $B = 0$ due spin-orbital interactions and the Jahn-Teller effect. The blue arrows indicate optically allowed transitions (spin conserving). The energy splitting values are taken from [27]. In **c)** (*green*), the level splitting due to the Zeeman effect is shown.

The most studied charge state of the color center is the SnV^- state, with photoluminescence at roughly $\lambda \approx 619\,\text{nm}$. The SnV^- can ionize and thereby change its charge state [28]. In this thesis, the SnV^- state was studied and always meant when referring to the SnV.

In Fig. 2.1.3, the energy level structure of the SnV^- is shown. Without an external magnetic field ($B = 0$), the ground and excited state are both split in an upper and lower branch due to spin-orbit coupling and the Jahn-Teller effect [28]. The respective transitions between those states are shown in Fig. 2.1.3 b). An external magnetic field lifts the two-fold degeneracy of

the states due to the Zeeman effect (see Fig. 2.1.3 c)).

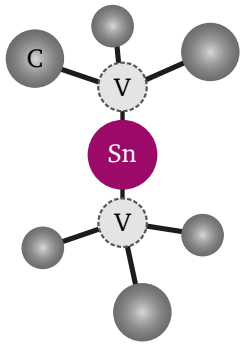

Figure 2.1.4: Atomic structure of a SnV center in the carbon lattice adapted from Ruf [7]. The tin (Sn) atom is marked in purple, the vacant lattice site (V) in a light gray, and the carbon (C) atoms in dark gray. The D_{3d} inversion symmetry of the color center leads to an first order insensitivity to electric fields.

Phonon-mediated transitions between the upper and lower branch of the ground state lead to a sub-microsecond spin coherent times even at cryogenic temperatures at $\approx 4\,\mathrm{K}$ [28]. This limitation can be overcome by further cooling the system down.

2.1.3 OPTICAL LINEWIDTH

The linewidth of an optical emitter is fundamentally limited by its lifetime τ, which can be evaluated by Fourier-transforming such an exponential decay, leading to

$$\Gamma_0 = \frac{1}{2\pi\tau}. \tag{2.1.1}$$

In addition to this natural broadening, we consider two other broadening effects, namely dephasing and spectral diffusion. The first is caused by noise that is rapid in comparison to the lifetime of the emitter, while the latter describes the contribution of noise on comparatively longer time scales. The fluctuations in the charge environment significantly contribute to spectral diffusion as a result of the Stark effect.

2.2 PURCELL ENHANCEMENT OF AN EMITTER IN AN OPTICAL CAVITY

The branching ratio into the ZPL is defined as the ratio between the emission into the ZPL and the total emission

$$\beta_0 = \frac{\gamma_{\mathrm{ZPL}}}{\gamma_{\mathrm{ZPL}} + \gamma_{\mathrm{PSB}} + \gamma_{\mathrm{dark}}}. \tag{2.2.1}$$

For the NV center, this branching ratio into the ZPL $\beta_0 \approx 3\,\%$ [3, 4], also called Debye-Waller factor, is quite low. The SnV centers Debye-Waller factor $\beta_0 \approx 57\,\%$ [29] is substantially higher, but still, a considerable part is emitted into the PSB. As described in the introduction, this poses a limitation on the achievable entanglement rate of the NV center as a quantum network node, as only ZPL photons can be utilized for this task [17]. However, the emission into the ZPL can be enhanced by coupling the emitter to an optical cavity mode and utilizing the Purcell effect [30]. The emitted photons from the Purcell-enhanced decay channel are moreover emitted into the cavity mode, which allows for a higher collection efficiency.

2.2.1 TRANSITION RATE IN A HOMOGENEOUS MATERIAL

To derive the implications of the Purcell effect, first, a look at the spontaneous emission rate of an emitter in a homogeneous material is needed. Any emitters spontaneous emission rate is given by Fermi's golden rule [31]

$$\gamma_{\mathrm{i}\to\mathrm{f}} = \frac{2\pi}{\hbar^2}\left|\langle f_\mathrm{k}|\hat{\mathscr{H}}_\mathrm{int}|i\rangle\right|^2 D(\omega_\mathrm{k}), \tag{2.2.2}$$

with $D(\omega_\mathrm{k})$ being the density of photon states at the angular frequency ω_k, and $\hat{\mathscr{H}}_\mathrm{int} = -\vec{d}\cdot\vec{E}$ being the interaction Hamiltonian between the emitter and the photon vacuum. $|i\rangle = |e\rangle\otimes|0\rangle$ is the initial state of the system. The emitter is in the excited state $|e\rangle$, and there is no photon present $|0\rangle$. After the photon emission the state is given by $|f_\mathrm{k}\rangle = |g\rangle\otimes|1_\mathrm{k}\rangle$, where the emitter is in the ground state $|g\rangle$ and a photon with a wave vector k is emitted $|1_\mathrm{k}\rangle$. For the case of emitted photons with considerably larger wavelength than the dimensions of the emitter, the dipole approximation can be used, leading to the transition rate [32]

$$\gamma_{\mathrm{i}\to\mathrm{f}} = \frac{\pi\omega_\mathrm{k}}{\hbar\epsilon_0\epsilon_\mathrm{r}V_0}\mu_\mathrm{ge}^2|\vec{d}\cdot\vec{e}|^2 D(\omega_\mathrm{k}) = 2\pi g^2|\vec{d}\cdot\vec{e}|^2 D(\omega_\mathrm{k}), \tag{2.2.3}$$

with the emitter-field coupling

$$g = \sqrt{\frac{\omega_\mathrm{k}\mu_\mathrm{ge}^2}{2\hbar\epsilon_0\epsilon_r V_0}}. \tag{2.2.4}$$

ϵ_0 and ϵ_r are the vacuum permittivity and the materials relative permittivity, μ_ge is the transition matrix element, V_0 the quantization volume, $\vec{e}$ the electric field polarization and $\vec{d}$ the dipole orientation. The photon density of states in a homogeneous medium with refractive index n is given as [7, 33]

$$D_\mathrm{hom}(\omega_\mathrm{k}) = \frac{\omega_\mathrm{k}^2 V_0 n^3}{\pi^2 c^3}, \tag{2.2.5}$$

with the speed of light c. By taking the average dipole overlap $|\vec{d}\cdot\vec{e}|^2 = 1/3$ into account, this leads to a spontaneous transition rate in a homogeneous material of

$$\gamma_\mathrm{hom} = \left(\frac{n\omega_\mathrm{k}}{c}\right)^3 \frac{\mu_\mathrm{ge}^2}{3\pi\hbar\epsilon_0\epsilon_\mathrm{r}}. \tag{2.2.6}$$

2.2.2 TRANSITION RATE IN AN OPTICAL CAVITY

As Eq. (2.2.2) indicates, increasing the density of states leads to a higher transition rate. A method of achieving this increase in the density of states is by embedding the emitter into an optical cavity. An elementary optical cavity is formed by two mirrors separated by the distance L_cav and is called a Fabry-Pérot resonator. An electromagnetic field inside the cavity interferes constructively if the cavity length is a multiple of the wavelength $\lambda = c/(n\cdot f)$ of the mode:

$$L_\mathrm{cav} = m\frac{\lambda}{2} = m\frac{c}{2nf}, \tag{2.2.7}$$

where f is the frequency and m the mode number. For a fixed cavity length L_{cav}, the distance in frequency between two modes m and $m+1$ can be derived from Eq. (2.2.7) and is called free spectral range (FSR):

$$f_{\text{FSR}} = \frac{c}{2nL_{\text{cav}}}. \tag{2.2.8}$$

For a cavity where the mirrors are not perfectly reflective, the mode has a finite lifetime, parameterized by a decay rate κ_{cav}. This leads to broadening in frequency of the cavity mode because the Fourier transform of an exponential decay leads to a Lorentzian-shaped spectral line with the full width at half maximum (FWHM) $\Gamma_{\text{cav}} = \kappa_{\text{cav}}/(2\pi)$ [32]. The

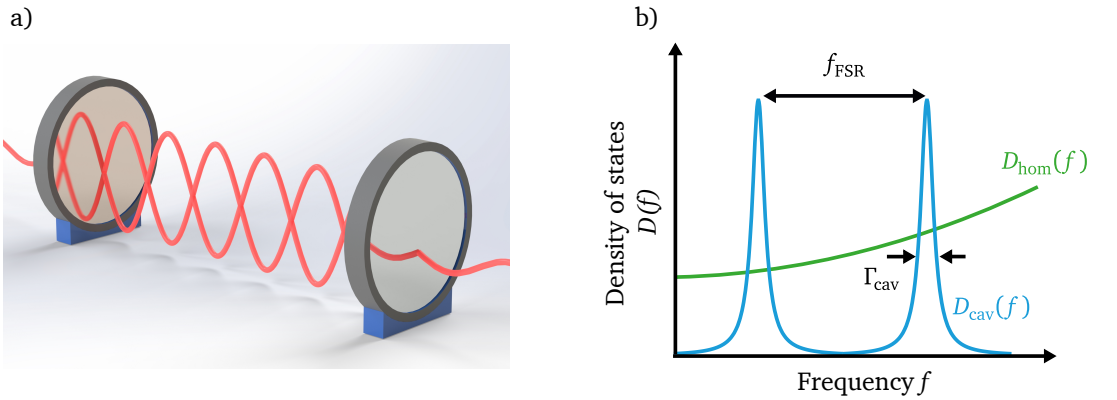

Figure 2.2.1: Adapted from Ruf [7]. **a)** Depiction of a Fabry-Pérot cavity with a standing wave between the two mirrors. **b)** Density of states over frequency in a homogeneous material (*green line*) and inside an optical cavity *light blue line*. The fundamental modes of the cavity, which are spaced in frequency by the FSR f_{FSR}, lead to Lorentzian peaks in the density of states. The cavity linewidth Γ_{cav} is a consequence of the decay rate κ of the cavity, which describes the escape time of the electromagnetic field through the mirrors with non-perfect reflectivity.

density of states of a Fabry-Pérot cavity is therefore given by equally spaced Lorentzians at the resonance frequencies f_m, with the linewidth Γ_{cav} as shown in Fig. 2.2.1 b). Around the resonance frequency f_0, this can be expressed as

$$D_{\text{cav}}(f) = \frac{1}{2\pi^2} \frac{\frac{\Gamma_{\text{cav}}}{2}}{(f-f_0)^2 + (\frac{\Gamma_{\text{cav}}}{2})^2}. \tag{2.2.9}$$

A maximum of the density of state can therefore be found at the resonance frequency f_0 leading to

$$D_{\text{cav}}(f_0) = \frac{1}{\pi^2 \Gamma_{\text{cav}}}. \tag{2.2.10}$$

2.2.3 PURCELL ENHANCEMENT

The enhancement of the transition rate can now be obtained by comparing the transition rate coupled to a cavity and in a homogeneous material. This boils down to a comparison of the density of states Eqs. (2.2.5) and (2.2.9) and the dipole overlap, as the rest of the equations are identical. This enhancement is quantified by the Purcell factor [30]

$$F_{\text{p}} = \frac{\gamma_{\text{cav}}}{\gamma_{\text{hom}}} = \frac{\zeta^2}{1/3} \frac{D_{\text{cav}}(f_0)}{D_{\text{hom}}(f_0)} \tag{2.2.11}$$

$$= 3\zeta^2 \frac{1}{\pi^2 \Gamma_{\text{cav}}} \frac{c^3}{4V_0 n^3 f^2}. \tag{2.2.12}$$

By introducing the quality factor $Q = f/\Gamma_{\text{cav}}$, the equation can be written as

$$F_{\text{p}} = 3\zeta^2 \frac{c^3}{4\pi^2 n^3 f^3} \frac{Q}{V_0}. \tag{2.2.13}$$

$\zeta = |\vec{d} \cdot \vec{e}|$ indicates the overlap between the dipole moment of the electronic transition $\vec{d}$ and the polarization of mode in the cavity $\vec{e}$. In Section 2.3 the mode volume for a Gaussian cavity mode is introduced as $V_0 = \pi\omega_0^2 L_{\text{cav}}/4$, with the beam-waste ω_0.

A commonly used parameter, which describes how often the light bounces between the cavity before it is lost, is the finesse. The finesse is inversely proportional to the total amount of cavity losses per round trip

$$\mathscr{F} = \frac{2\pi}{\mathscr{L}_{\text{tot}}} = \frac{f_{\text{FSR}}}{\Gamma_{\text{cav}}}. \tag{2.2.14}$$

By using Eqs. (2.2.8) and (2.2.14), and the expression for the mode volume V_0, an alternative representation of the Purcell factor can be found

$$F_{\text{p}} = \frac{6}{\pi^3} \frac{\zeta\lambda^2}{n^2} \cdot \frac{\mathscr{F}}{\omega_0^2}. \tag{2.2.15}$$

This shows that the Purcell factor linearly depends on the finesse and, therefore, inversely to the amount of cavity losses $\mathscr{L}_{\text{tot}}$.

2.2.4 ENHANCED BRANCHING RATIO

The relevant parameter for increasing the entanglement rate of the color center as a potential quantum network node is the branching ratio into the cavity mode β_{cav}, which is defined as the ratio between the emission into the cavity mode and the total emission. For deriving that ratio, a look at the decay rates through different channels from the excited state to the ground state need to be considered.

THE NV CENTER

For the NV center, the radiative emission from the $E_{\text{x,y}}$ state to the ground state, with the decay rate γ_{rad}, is split into a ZPL emission fraction β_0 and a PSB emission fraction $(1-\beta_0)$. Here, β_0 is the Debye-Waller factor, which is measured for the NV center to be $\beta_0 \approx 3\,\%$ [3, 4]. Additionally, decay via transitions through the singlet state can occur, which is modeled as non-radiative decay at rate γ_{dark}. without coupling to a cavity, The total decay rate of the NV center is therefore given by

$$\gamma_0 = \beta_0\gamma_{\text{rad}} + (1-\beta_0)\gamma_{\text{rad}} + \gamma_{\text{dark}}. \tag{2.2.16}$$

As introduced above, if the ZPL transition is now coupled to a mode of a cavity, another decay channel is opened, leading to a total decay rate of

$$\gamma' = F_{\text{P}}^{\text{ZPL}}\beta_0\gamma_{\text{rad}} + \beta_0\gamma_{\text{rad}} + (1-\beta_0)\gamma_{\text{rad}} + \gamma_{\text{dark}}. \tag{2.2.17}$$

The branching ratio into the cavity mode is then calculated by the ratio between the Purcell-enhanced decay rate into the cavity mode and the total decay rate

$$\beta_{\text{cav}} = \frac{F_{\text{P}}^{\text{ZPL}}\beta_0\gamma_{\text{rad}}}{\gamma'} = \frac{F_{\text{P}}^{\text{ZPL}}\beta_0}{F_{\text{P}}^{\text{ZPL}}\beta_0 + \frac{\gamma_{\text{dark}}+\gamma_{\text{rad}}}{\gamma_{\text{rad}}}}. \tag{2.2.18}$$

The ratio between radiative decay and non-radiative decay is defined as the quantum efficiency $\eta = \gamma_{\text{rad}}/(\gamma_{\text{dark}} + \gamma_{\text{rad}})$, which can be substituted to obtain

$$\beta_{\text{cav}} = \frac{F_{\text{P}}^{\text{ZPL}}\beta_0\eta}{F_{\text{P}}^{\text{ZPL}}\beta_0\eta + 1}. \tag{2.2.19}$$

THE SNV CENTER

For the SnV center, the branching ratio into the cavity mode can be derived in the same way as for the NV center, with some additional considerations. Here, Purcell enhancement of the C transition is considered. From the lower branch of the excited state, radiative transitions to the upper and lower branch of the ground state, with decay rates γ_{C} and γ_{D} take place ($\gamma_{\text{rad}} = \gamma_{\text{C}} + \gamma_{\text{D}}$). The branching ratio into the C transition was measured as $\alpha = \gamma_{\text{C}}/(\gamma_{\text{C}} + \gamma_{\text{D}}) \approx 80\,\%$ [2]. The total decay rate coupled to a cavity resonant to the C transition is then given as

$$\gamma' = F_{\text{P}}^{\text{ZPL}}\beta_0\gamma_{\text{C}} + \beta_0(\gamma_{\text{C}} + \gamma_{\text{D}}) + (1-\beta_0)(\gamma_{\text{C}} + \gamma_{\text{D}}) + \gamma_{\text{dark}}. \tag{2.2.20}$$

The branching ratio into the cavity mode can then be derived in the same way as for the NV center. By substituting the quantum efficiency η and the branching ratio into the C transition α, the cavity mode branching ratio can be expressed as

$$\beta_{\text{cav}} = \frac{F_{\text{P}}^{\text{ZPL}}\beta_0\eta\alpha}{F_{\text{P}}^{\text{ZPL}}\beta_0\eta\alpha + 1}. \tag{2.2.21}$$

The quantum efficiency of the SnV is stated in literature as $\eta \approx 80\,\%$ [28] and the Debye-Waller factor as $\beta_0 \approx 57\,\%$ [29].

2.3 A FABRY-PÉROT OPEN MICROCAVITY

In this section, a closer look at open microcavities is taken. First, key parameters of a bare cavity are retrieved from a one-dimensional matrix model. Then, introducing a diamond layer into the cavity is studied using the same model, and a brief introduction to the Gaussian mode inside a plane-concave cavity is given. It is possible using those models to extract multiple cavity parameters from detecting the transmission through the cavity, as detailed in Chapter 5. A more detailed description and derivations can be found in [32].

2.3.1 ONE-DIMENSIONAL TRANSFER-MATRIX MODEL

A BARE CAVITY

In the previous section, key parameters of a Fabry-Pérot cavity, for example, the resonance condition or the finesse, are used. Using a one-dimensional transfer-matrix model, we can derive those parameters [32]. In this model, the electric field is split into a forward propagating mode $E_{\rightarrow}(z)$ and a backward propagating mode $E_{\leftarrow}(z)$ ($E = E_{\rightarrow} + E_{\leftarrow}$). Matrices then describe the propagation through media and the behavior at dielectric interfaces. In this way, the initial electric field E can be related to the electric field at a distance d along the propagation axis

$$\begin{pmatrix} E_{\rightarrow} \\ E_{\leftarrow} \end{pmatrix} = \underbrace{\begin{pmatrix} e^{ikd} & 0 \\ 0 & e^{-ikd} \end{pmatrix}}_{\mathbf{P}} \begin{pmatrix} E'_{\rightarrow} \\ E'_{\leftarrow} \end{pmatrix}, \tag{2.3.1}$$

where $k = 2\pi n/\lambda_0$ is the wave vector. The transition from a material with refractive index n_1 to another with refractive index n_2 can be described by

$$\begin{pmatrix} E_{\rightarrow} \\ E_{\leftarrow} \end{pmatrix} = \underbrace{\frac{1}{\tau_{12}} \begin{pmatrix} 1 & \rho_{12} \\ \rho_{12} & 1 \end{pmatrix}}_{\mathbf{I}} \begin{pmatrix} E'_{\rightarrow} \\ E'_{\leftarrow} \end{pmatrix}, \quad \text{with} \quad \rho_{12} = \frac{n_1 - n_2}{n_1 + n_2}; \quad \tau_{12} = \frac{2n_1}{n_1 + n_2}. \tag{2.3.2}$$

A model cavity can be described by multiplying these matrices, which we will use later to simulate the electric field distribution in a hybrid cavity. However, to derive the resonance condition of the bare cavity, we introduce another matrix directly describing a mirror for simplification:

$$\mathbf{M} = \frac{1}{t} \begin{pmatrix} 1 & r \\ r & 1 \end{pmatrix}, \tag{2.3.3}$$

with the transmission and reflection coefficients t and r. Therefore, a bare cavity of length L_{cav} can then be described by

$$\mathbf{M}_{\text{bc}} = \mathbf{M}_2 \mathbf{P}_{\text{air}} \mathbf{M}_1 = \frac{1}{t_2} \begin{pmatrix} 1 & r_2 \\ r_2 & 1 \end{pmatrix} \begin{pmatrix} e^{ikL_{\text{cav}}} & 0 \\ 0 & e^{-ikL_{\text{cav}}} \end{pmatrix} \frac{1}{t_1} \begin{pmatrix} 1 & r_1 \\ r_1 & 1 \end{pmatrix}, \tag{2.3.4}$$

with $\mathbf{M}_1$, $\mathbf{M}_2$ describing the two mirrors and $\mathbf{P}_{\text{air}}$ the air gap between them.

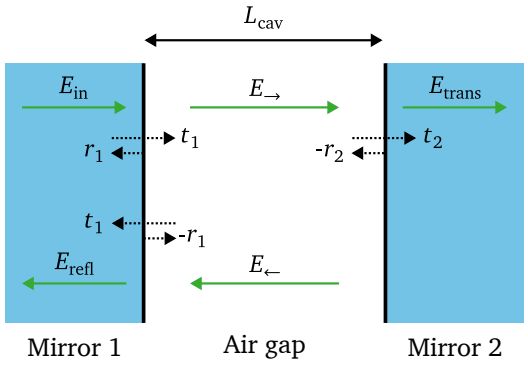

Figure 2.3.1: Adapted from van Dam [32]. Depiction of a one-dimensional cavity model analyzed with the transfer matrix model. The electric field is split into forwards ($E_{\rightarrow}$, E_{in}, E_{trans}) and backwards ($E_{\leftarrow}$, E_{refl}) propagating modes. The transmission and reflection at the mirrors are given by the parameters t_1, t_2 and r_1, r_2.

To find the resonance condition of the cavity, the cavity transmission needs to be considered. The incident field E_{in}, and the reflected field E_{refl} are defined (see Fig. 2.3.1), such that they relate via

$$\begin{pmatrix} E_{\text{in}} \\ E_{\text{refl}} \end{pmatrix} = \mathbf{M}_{\text{bc}} \begin{pmatrix} E_{\text{trans}} \\ 0 \end{pmatrix} \tag{2.3.5}$$

to the transmitted electric field E_{trans}, assuming there is no incidence electric field from the right. This leads to a total transmittance of

$$T = \left| \frac{E_{\text{trans}}}{E_{\text{in}}} \right|^2 = \left| \frac{1}{\mathbf{M}_{\text{bc}[1,1]}} \right|^2 = \frac{|t_1|^2 |t_2|^2}{|e^{ikL_{\text{cav}}} - r_1 r_2 e^{-ikL_{\text{cav}}}|^2} \tag{2.3.6}$$

$$= \frac{|t_1|^2 |t_2|^2}{(1 - r_1 r_2)^2 \left(1 + \left(\frac{2\mathcal{F}}{\pi} \sin(kL_{\text{cav}})\right)^2\right)}. \tag{2.3.7}$$

In the last step, the finesse is introduced and defined as

$$\mathscr{F} = \frac{\pi\sqrt{r_1 r_2}}{1 - r_1 r_2} \approx \frac{2\pi}{\mathscr{L}_1 + \mathscr{L}_2}, \tag{2.3.8}$$

with the approximation being reasonable for highly reflective mirrors [32]. $\mathscr{L}_1$, $\mathscr{L}_2$ are the losses through the mirrors. Now, using Eq. (2.3.6), the resonance condition can be found by maximizing the transmission T, leading to

$$L_{\text{cav}} = \frac{mc}{2nf}, \quad \text{with} \quad m \in \mathbb{N}. \tag{2.3.9}$$

Also from Eq. (2.3.6), the width of the resonance peak can be derived, leading to a FWHM of

$$\Gamma_{\text{cav}} = \frac{c}{2nL_{\text{cav}}\mathscr{F}} = \frac{f_{\text{FSR}}}{\mathscr{F}}, \tag{2.3.10}$$

with the previously introduced FSR (see Eq. (2.2.8)). This relates the finesse to the FSR. The equation is also used to calculate the finesse $\mathscr{F}$ from the cavity length L_{cav} and the cavity linewidth Γ_{cav}, which can be retrieved from measurements (see Chapter 5).

A HYBRID CAVITY

So far, only an analysis of a bare cavity has been done. However, we have a diamond in the cavity for our experiments, introducing a layer with a drastically different refractive index than air. We can model this alteration in the same way as for the bare cavity using the transfer-matrix model [32]

$$\mathbf{M}_{\text{hc}} = \mathbf{M}_2\mathbf{P}_{\text{dia}}\mathbf{I}_{\text{air}\to\text{dia}}\mathbf{P}_{\text{air}}\mathbf{I}_{\text{dia}\to\text{air}}\mathbf{M}_1, \tag{2.3.11}$$

with $\mathbf{M}_1$, $\mathbf{M}_2$ (see Eq. (2.3.3)) describing the mirrors, $\mathbf{I}_{\text{air}}$, $\mathbf{I}_{\text{dia}}$ describing the transitions between air and diamond (see Eq. (2.3.2)), and $\mathbf{P}_{\text{air}}$, $\mathbf{P}_{\text{dia}}$ the propagation trough the air and diamond layer (see Eq. (2.3.1)). As for the bare cavity, the total cavity transmission T can be derived, leading to a new resonance condition

$$(n_{\text{air}} + n_{\text{dia}})\sin\left(\frac{2\pi f}{c}(n_{\text{air}}L_{\text{air}} + n_{\text{dia}}L_{\text{dia}})\right) = (n_{\text{air}} - n_{\text{dia}})\sin\left(\frac{2\pi f}{c}(n_{\text{air}}L_{\text{air}} - n_{\text{dia}}L_{\text{dia}})\right), \tag{2.3.12}$$

with the air and diamond lengths L_{air} and L_{dia}. This equation cannot be solved analytically for the resonance frequencies f_m. However, for high mode numbers, an approximation can be made by expressing f as the resonance frequencies of a bare cavity with a small deviation $f \approx mc/(2n_{\text{air}}L_{\text{air}} + 2n_{\text{dia}}L_{\text{dia}}) + \Delta f$ [34]. By substituting this expression into Eq. (2.3.12) and neglecting Δf on the right side of the equation, the resonance frequencies

$$f_m = \frac{c}{2\pi(n_{\text{air}}L_{\text{air}} + n_{\text{dia}}L_{\text{dia}})}\left(m\pi - (-1)^m \arcsin\left(\frac{n_{\text{dia}} - n_{\text{air}}}{n_{\text{dia}} + n_{\text{air}}}\sin\left(m\pi\frac{n_{\text{air}}L_{\text{air}} - n_{\text{dia}}L_{\text{dia}}}{n_{\text{air}}L_{\text{air}} + n_{\text{dia}}L_{\text{dia}}}\right)\right)\right) \tag{2.3.13}$$

can be found, where $m \in \mathbb{N}$ is the mode number.

When plotted over the air gap L_{air}, as shown in Fig. 2.3.2, a hybridized patter of "only-air-cavity mode" $f_{\text{air}} = m_{\text{air}}c/(2n_{\text{air}}L_{\text{air}})$ and "only-diamond-cavity mode" $f_{\text{dia}} = (2m_{\text{dia}} - 1)c/(4n_{\text{dia}}L_{\text{dia}})$ with avoided crossings is visible. There can be two special cases considered for the hybrid mode: An air-like mode, where the hybrid modes intersect with the "air-only

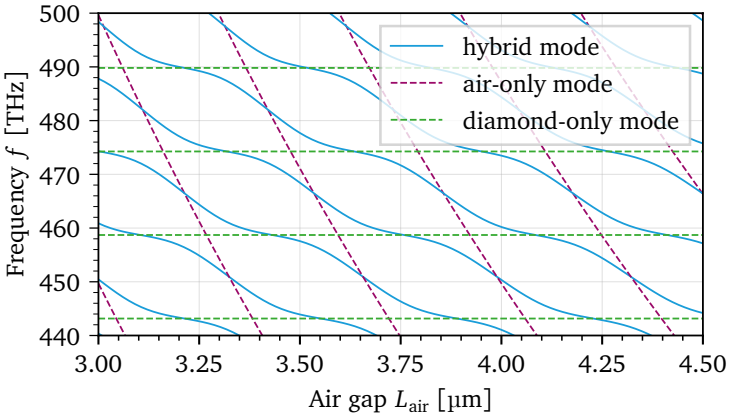

Figure 2.3.2: Resonance frequencies of a hybrid diamond-air cavity plotted over the length of the air gap L_{air} (*blue line*). In addition, the resonance frequencies for an air-only (dotted purple line, $f = m_{air}c/(2\pi n_{air}L_{air})$) and a diamond-only (dotted green line, $f = (2m_{dia}-1)c/(4\pi n_{dia}L_{dia})$ mode are displayed.

modes", and an air-like mode, where the hybrid modes intersect with the "diamond-only modes". Fig. 2.3.2 also shows that the slope $\delta f/\delta L_{air}$ is smallest for the diamond-like mode, rendering it less sensitive to vibrations. The conditions for those modes are given by [32]:

$$L_{dia} = m_{dia}\frac{\lambda_0}{2n_{dia}} \quad \text{and} \quad L_{air} = m_{air}\frac{\lambda_0}{2n_{air}}; \qquad \text{(air-like mode)} \tag{2.3.14}$$

$$L_{dia} = (2m_{dia}+1)\frac{\lambda_0}{4n_{dia}} \quad \text{and} \quad L_{air} = (2m_{air}+1)\frac{\lambda_0}{4n_{air}}; \qquad \text{(diamond-like mode)} \tag{2.3.15}$$

Those conditions show that the diamond thickness L_{dia} defines the possible modes of the cavity as it is in an experimental setup not tuneable compared to the air gap length L_{air}. For an air-like mode, the electric field has a node at the air-diamond interface, while in a diamond-like mode, an anti-node is located at the interface (see Fig. 2.3.3).

ELECTRIC FIELD DISTRIBUTION Finally, we take a look at the electric field distribution in a hybrid diamond-air cavity. As suggested earlier, in Eq. (2.3.11), the matrices describing the mirrors are replaced by layers of alternating reflective indices to simulate Bragg mirrors. The electric field distribution inside the cavity $|E_{\rightarrow}+E_{\leftarrow}|(z)$ can then be calculated numerically, as shown in [32]. The electric field distribution for air-like and diamond-like modes are shown in Fig. 2.3.3a,b). This numerical evaluation shows that the electric field is more confined inside the diamond for a diamond-like mode, compared to the air-like mode.

To describe the linewidth and the FSR of the hybrid cavity, the definition of the effective cavity length L_{eff} is introduced [35],

$$L_{eff} = 2\frac{\int_{cav} n^2(z)|E(z)|^2\,dz}{n_{dia}^2\left|E_{max,dia}\right|^2}, \tag{2.3.16}$$

with the maximum of the electric field in the diamond $E_{max,dia}$. The integral is evaluated over the whole cavity, including the Bragg mirrors. Using this definition of the effective length, the cavity linewidth of such a hybrid is then given as [32]

$$\Gamma_{cav} = \frac{c}{2n_{dia}L_{eff}\mathscr{F}} = \frac{f_{FSR}}{\mathscr{F}}. \tag{2.3.17}$$

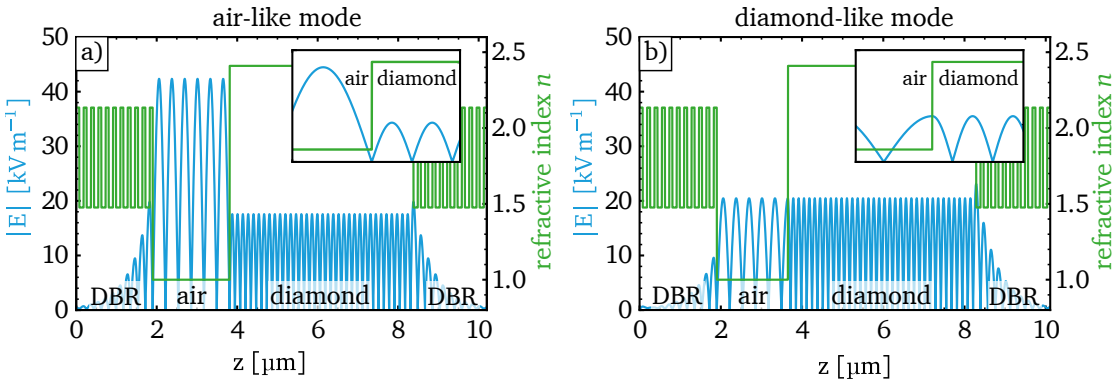

Figure 2.3.3: Distribution of the electric field in the cavity adapted from van Dam [32]. **a)** Here, the electric field distribution of an air-like mode is shown. In the zoomed-in box, the positioning of an anti-node at the diamond-air interface is clearly visible. In **b)**, the electric field distribution for an diamond-like mode is shown, with a node at the diamond-air interface.

2.3.2 GAUSSIAN BEAM OPTICS

So far, only a one-dimensional model has been introduced, neglecting the lateral extension of the electric field. The cavity in the shown experiments consists of a plane mirror and an approximately spherical concave mirror. A more detailed description of the Gaussian beam optics in such a cavity can be found in [32]; here, just the most important parameters are stated. As shown in Eq. (2.2.13), for the Purcell factor, the mode Volume is an important parameter, which can be derived as [7, 36]

$$V_0 = \frac{\pi \omega_0^2}{4} L_{\text{eff}}, \tag{2.3.18}$$

describing the mode volume in a bare cavity, with a correction introduced by the effective length. ω_0 is the Gaussian beam waste, which can be derived for a bare cavity by using wave optics and considering the boundary conditions of the plane and concave mirrors [36]

$$\omega_0 = \sqrt{\lambda_0/\pi}\sqrt[4]{L(\text{ROC} - L_{\text{cav}})}, \tag{2.3.19}$$

with the rate of curvature (ROC) of the concave mirror, the wavelength in vacuum λ_0 and the cavity length L_{cav}.

For the hybrid cavity, two Gaussian beams, one located in the diamond and one located in the air, can be considered to derive a similar equation to 2.3.19 [32]. The found expression is similar to the expression for a bare cavity (Eq. (2.3.19)), with a correction for the cavity length term, weighted by the reflective indices of diamond and air [32]:

$$\omega_0 = \sqrt{\lambda_0/\pi}\sqrt[4]{L(\text{ROC} - L')}, \quad \text{with} \quad L' = L_{\text{air}} + \frac{n_{\text{air}}}{n_{\text{dia}}} L_{\text{dia}}. \tag{2.3.20}$$

3 | FABRICATION OF DIAMOND SAMPLES

In this chapter, a design and a fabrication method for color center-enriched, micrometer-thin diamond platelets for use in an open microcavity is presented. A diamond platelet is denoted as a single-digit, micrometer-thin sample with side lengths of tens of micrometers. In this thesis, two different fabrication methods were studied to obtain these diamond platelets, namely electron beam (e-beam) lithography with dry etching and laser cutting. Fabrication parameters were varied and optimized. Parameters that are varied over different fabrication runs are indicated by referring to ranges of these values. A detailed description for every fabrication step can be found in the Appendix A. In the second part of the chapter, the bonding process of diamond platelets to a Bragg mirror is outlined, and a proposed method to increase the bonding yield is discussed.

The main motivation for fabricating platelets instead of thinning down the entire membrane, as shown in [18, 37], lies in the bonding behavior. Previous work [7], as well as attempts made during this thesis, have shown that bonding a 2 mm × 2 mm diamond membrane to a Bragg mirror is challenging. Since the bonding of the platelet or membrane is dominated by Van der Waals forces, close contact between the surfaces is essential due to the attractive force's inverse proportionality to the sixth power of the distance, $F_{\mathrm{vdW}} \propto d^{-6}$. One reason for the lack of close contact of 2 mm × 2 mm membranes could be the presence of small dust particles between the two surfaces. The smaller bonding area of platelets might mitigate this issue due to the reduced clean area required. Another factor is that tens of platelets can be fabricated from a single membrane, enabling multiple bonding attempts without requiring intermediate cleaning steps, as required for multiple bonding attempts with the whole membrane. A usable sample is already obtained if a subset of those platelets bond successfully.

3.1 40-µm DIAMOND MEMBRANES CONTAINING EMITTERS

As a starting substrate, a 2 mm × 2 mm × 0.5 mm, single crystal, chemical vapor deposition (CVD) grown bulk diamond in {100} face orientation is used (Element Six EL SC Plate). In the first step, diamond samples are sliced and polished into diamond membranes with a thickness of $d \approx (30-50)\,\mu\mathrm{m}$ as well as enriched with color centers.

3.1.1 SLICING, POLISHING, AND SURFACE TREATMENT

The bulk diamond sample is laser sliced into three diamond membranes. After chemical-mechanical polishing, a diamond membrane is approximately $d \approx 40\,\mu\mathrm{m}$ thick and has a surface roughness lower then $R_{\mathrm{q}} < 1\,\mathrm{nm}$ (*executed and specified by Almax easyLab*).

STRAIN RELIEF ETCH

A dry etch is performed on the diamond membranes to further reduce the surface roughness and relief strain introduced by the polishing process. Two different types of etch methods were performed on various samples. The standard procedure, used on all samples except one (*Pai Mei*), consists of an argon-chlorine (Ar/Cl_2) etch, followed by an oxygen (O_2) etch. Both etches are aimed to remove the same amount of material with a total depth of $d \approx (3-8)\,\mu m$.

In a second method, based on the work of [18, 37], multiple Ar/Cl_2 and O_2 etches are interleaved. First, a $\Delta t = 50\,min$ initial Ar/Cl_2 etch is performed, with an expected removal of $d \approx 1.75\,\mu m$ of diamond, followed by an $\Delta t = 5\,min$, $d \approx 1.25\,\mu m$ O_2 etch. Afterwards, Ar/Cl_2 etches ($\Delta t = 15\,min$, $d \approx 0.5\,\mu m$) are interleaved with O_2 etches ($\Delta t = 5\,min$, $d \approx 1.25\,\mu m$). This is repeated $N = 4$ times, ultimately resulting in an expected removal of $d \approx 10.1\,\mu m$ of material. The etch parameters are stated in Appendix A.

SURFACE ROUGHNESS In Fig. 3.1.1 a), a height map obtained by an atomic force microscope (AFM) measurement of a diamond membrane (*O-Ren Ishii*) after slicing and polishing is shown. A clear pattern, presumably introduced by the chemical-mechanical polishing, is visible. The root mean square (RMS) roughness calculated for the high-frequency components of the Fourier transformed surface ($f > 2\,\mu m^{-1}$) is $R_q \approx 0.5\,nm$. The surface profile measured on the top side of a diamond platelet (*Pai Mei*) where the strain relief etch with interleaved Ar/Cl_2 and O_2 chemistry is performed is shown in Fig. 3.1.1 b). The polishing pattern is no longer visible after performing the strain relief etch. The measurement also shows that the strain relief etch reduces the surface roughness, in this case, to $R_q \approx 0.2\,nm$. The two measured diamond samples at different fabrication stages were sliced from the same bulk substrate and polished in the same batch, allowing for a direct comparison across the samples while assuming similar behavior.

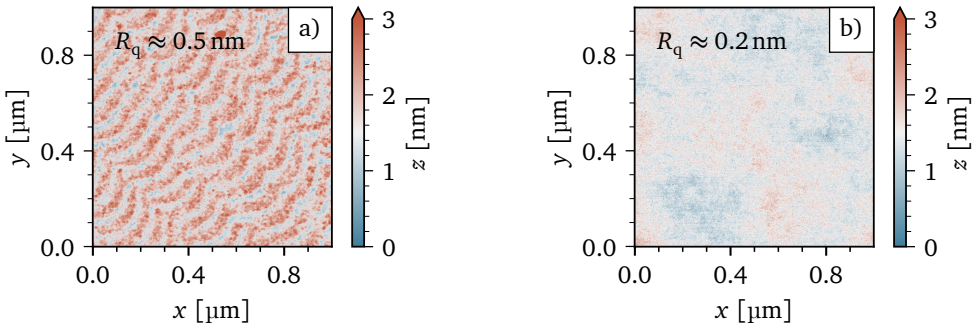

Figure 3.1.1: **a)** Surface profile of a diamond membrane (*O-Ren Ishii*) after slicing and polishing measured by an AFM. **b)** AFM measurement of a diamond platelet bond to a mirror (*Pai Mei*) on the side where a strain relief etch with interleaved Ar/Cl_2 and O_2 chemistry was performed. Comparing both images shows the reduction in surface roughness due to the strain relief etch.

3.1.2 ENRICHMENT WITH COLOR CENTERS

NV CENTERS The already abundant nitrogen in the bulk diamond ($\rho_N < 5\,ppm$ [38]), introduced during the CVD growing process, can be utilized for the creation of nitrogen-vacancy (NV) centers. Vacancies are introduced by irradiating the diamond with high-energy ($E_{e^-} \approx 2\,MeV$) electrons using a Van de Graaff electron accelerator (*Performed by the Reactor*

Institute of TU Delft). The density of the resulting NV centers can be controlled by adjusting the irradiation dose. A higher electron irradiation dose leads to a higher NV density for the same nitrogen concentration. However, achieving perfect control over the NV density is challenging, as the nitrogen concentration in the bulk diamond can vary between samples and even within a single sample. In this thesis, all NV samples were irradiated with a dose of $D_{e^-} \approx 4 \cdot 10^{13}\,\mathrm{e/cm^2}$. An annealing step is performed to merge nitrogen atoms and vacancies in the diamond, thus forming NV centers. A more detailed description of the annealing process is provided later in the text. This enrichment method yields an approximately uniform distribution of NV centers throughout the diamond. As a result, the NV center enrichment can be carried out before slicing, polishing, and applying surface treatments to the diamond.

SNV CENTERS To obtain tin-vacancy (SnV) centers in the substrate, tin ions are implanted into the diamond (*carried out by Innovion*) under an angle of $\alpha = 7°$. Here, a dose of $D_{\mathrm{Sn}} \approx 5 \cdot 10^{10}\,\mathrm{Sn/cm^2}$ and an irradiation energy of $E_{\mathrm{Sn}} \approx 350\,\mathrm{keV}$ is used leading to a depth distribution around $d_{\mathrm{Sn}} \approx 90\,\mathrm{nm}$ as simulated using the stopping and range of ions in matter (SRIM) [39] (see Fig. 3.1.2 a)). To prevent removing the implanted tin layer, irradiation is always performed after slicing, polishing, and the strain relief etch. After implantation, annealing is performed to create SnV centers by combining vacancies and tin ions, which were both introduced by the implantation.

ANNEALING Samples with future SnV and NV centers were annealed at high vacuum of $p < 10^{-6}\,\mathrm{mbar}$ to prevent oxidation. The annealing recipe is shown in Fig. 3.1.2 b). First,

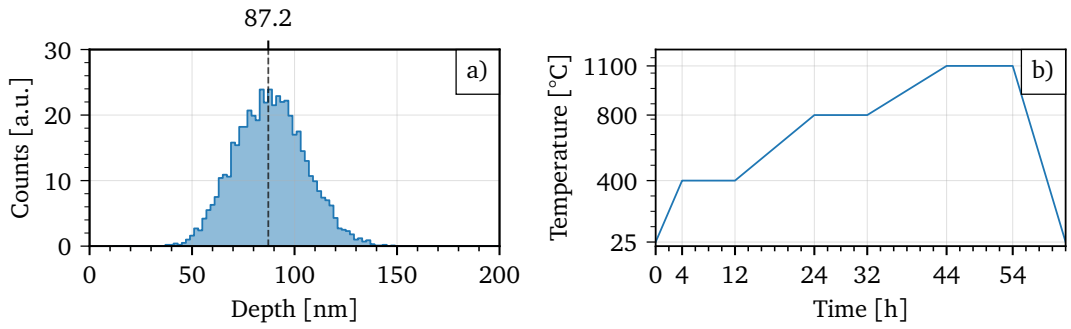

Figure 3.1.2: **a)** Depth distribution of tin ions in diamond for an implantation energy of $E_{\mathrm{Sn}} \approx 350\,\mathrm{keV}$ and an angle of incidence of $\alpha = 7°$, obtained by simulating $N = 5000$ tin ion trajectories in SRIM [39]. **b)** Temperatures over time for the recipe used to anneal NV and SnV samples.

the temperature is raised to $T_1 = 400\,°\mathrm{C}$ over the course of four hours and then kept at this temperature for eight hours. For twelve hours, the temperature is then increased to $T_2 = 800\,°\mathrm{C}$ and kept there for another eight hours. In the last step, the temperature is raised for twelve hours to the maximal value of $T_3 = 1100\,°\mathrm{C}$, where it is kept for ten hours before being cooled down to room temperature again. The temperature was raised in this slow manner to allow contaminants, which could get loose at rising temperatures, to be pumped out. Before and after annealing, a tri-acid clean at boiling temperature is performed (see Appendix A) to mitigate graphitization during the annealing process and remove nevertheless created graphite afterward.

3.2 µm THIN DIAMOND PLATELETS

In the next step, diamond platelets with a thickness of single-digit micrometers are fabricated. To achieve this, trenches with depths of $d \approx (7-15)\,\mu\text{m}$ are created around the perimeter of the future platelets using e-beam lithography and dry etching or laser cutting while leaving a holding bar in place. Subsequently, an etching process is performed on the backside of the membrane to remove material until the trenches are etched through, resulting in the formation of platelets that are held in place by the holding bar.

3.2.1 DESIGN

In Fig. 3.2.1, the fabrication design used to produce the diamond platelets is shown. The platelet designs are created asymmetrically to allow for the distinction of flipped platelets on the mirror. The design is arranged in rows of platelets, leaving wider bars to give the thinned-down part of the membrane structural support. In the initial fabrication runs, including all laser cut samples studied during this thesis, a design with smaller platelets featuring a surface area range of $A \approx (400-4900)\,\mu\text{m}$ was used. However, since the bonding yield with smaller platelets from these fabrication runs was lower than that with larger platelets, the platelet sizes were increased, and the design shown in Fig. 3.2.1 was adapted accordingly. In contrast to the earlier design with four quadrants (see Fig. 3.2.2), where in the middle of the membrane no platelets are placed, positioning in rows allows for achieving a larger range of platelet thicknesses due to the inhomogeneous thinning down achieved by the backside etch discussed in Section 3.2.2 and [7].

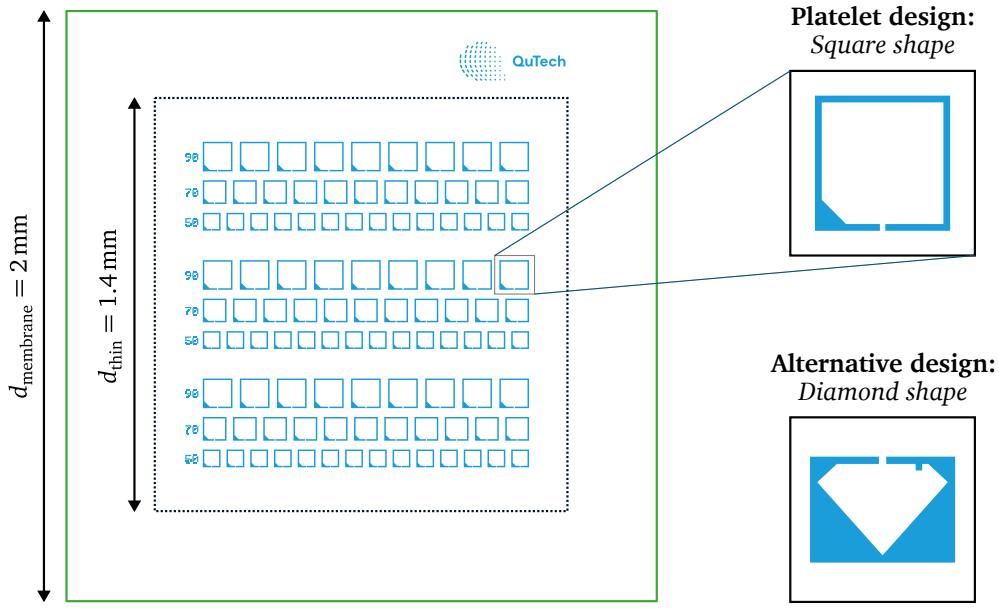

Figure 3.2.1: Design for the fabrication of µm-thin diamond platelets. The green outer line corresponds to the size of the diamond membrane, while the inner dotted black line outlines the area where the diamond gets thinned down through the backside etch. The light blue areas around the future platelets, inside the numbers, and making up the QuTech logo are µm-deep etched or laser-cut into the diamond membrane. The numbers next to every row indicate the edge length of the platelets in that row. On the right side, a zoomed-in view of a platelet structure is given, and an alternative diamond-shaped design is used in some fabrication runs for artistic reasons.

3.2.2 FABRICATION USING E-BEAM LITHOGRAPHY AND DRY ETCHING

One method for fabricating said trenches around the future platelets is using e-beam lithography and dry etching. For this process, after an initial piranha clean, a $d_{\mathrm{hm}} \approx 330\,\mathrm{nm}$ thin layer of silicon nitride (SiN_x) is deposited as a hard mask onto the membrane using plasma-enhanced chemical vapor deposition (PECVD). On top of the SiN_x hard mask, a thin layer $d_{\mathrm{res}} \approx 430\,\mathrm{nm}$ e-beam resist *CSAR-18* is spin coated, as well as a layer of *Elektra92* to reduce the effect of surface charging of the diamond during e-beam exposure (see Fig. 3.2.2 a)). For spin coating and further handling of the sample, the diamond membrane is glued to a $2\,\mathrm{cm} \times 2\,\mathrm{cm}$ silicon (Si) carrier piece with poly(methyl methacrylate) (PMMA). Afterwards, the sample is e-beam exposed and developed by dipping the sample into water ($\Delta t_{\mathrm{water}} = 1\,\mathrm{min}$) to remove the Electra92, then into the developers pentylacetade ($\Delta t_{\mathrm{pa}} = 1\,\mathrm{min}$) and xylene ($\Delta t_{\mathrm{xy}} = 5\,\mathrm{s}$), and finally into isopropyl alcohol (IPA) ($\Delta t_{\mathrm{ipa}} = 1\,\mathrm{min}$) for stopping the development and cleaning (see Fig. 3.2.2 b)). Subsequently, the pattern is transferred into the SiN_x hard mask using anisotropic inductively coupled plasma (ICP) reactive ion etching (RIE) with a CHF_3 chemistry, and a targeted depth of $d \approx 330\,\mathrm{nm}$. In order to ensure the complete etching of the hard mask, the etching duration is intentionally extended beyond the time required to attain the desired depth, providing an additional margin of safety for the process. Afterwards, the remaining resist is stripped in a *PRS 3000* bath for $\Delta t_{\mathrm{PRS}} \approx 12\,\mathrm{h}$ (see Figs. 3.2.2 c) and 3.2.3 a)). For the first $\Delta t_{\mathrm{PRS}} \approx 2\,\mathrm{h}$, the solution is heated to $T_{\mathrm{PRS}} = 80\,^{\circ}\mathrm{C}$ in a bain-marie. The PRS 3000 bath also separates the diamond membrane and the Si piece. After a piranha clean, an anisotropic ICP RIE with an oxygen (O_2) chemistry is used to transfer the pattern from the hard mask $d \approx 8\,\mu\mathrm{m}$ deep into the diamond membrane (see Fig. 3.2.3 b)). Therefore, the membrane is glued to a 4-inch SiO_2 carrier wafer using thermal paste. Then, to clean the diamond and remove the remaining SiN_x, a hydrofluoric acid (HF) clean is performed (see Fig. 3.2.2 d)).

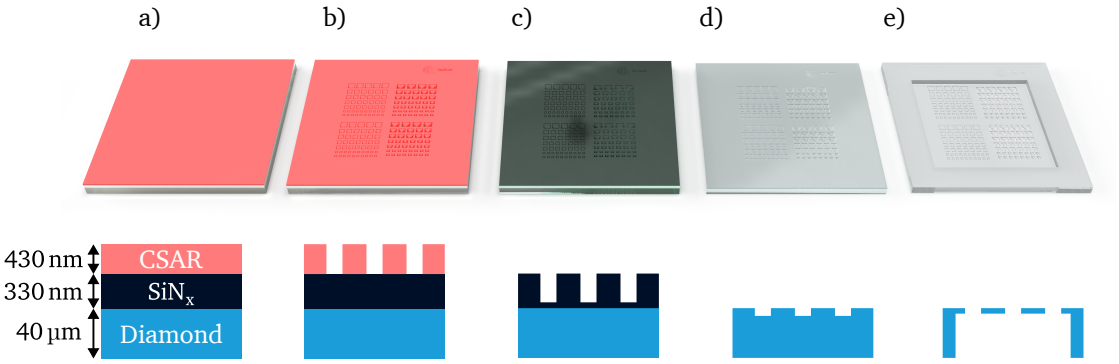

Figure 3.2.2: Three dimensional rendered image (*first row*) and two dimensional side view (*second row*) of diamond membranes after main fabrication steps. All depictions are not to scale. **a)** The diamond membrane with the hard mask and resist on top is displayed. The *Elektra92* layer is not depicted. In **b)**, the sample after e-beam exposure and development is shown. **c)** shows the membrane after the transfer CHF_4-etch into the SiN_x, while in **d)** the sample after the O_2 transfer etch into the diamond is shown. In **e)**, the final membrane with released diamond platelets held in place by the holding bars after the Ar/Cl_2 and O_2 backside etch is shown. A detailed description of all fabrication steps can be found in Appendix A

.

PLATELET RELEASE ETCH In the final fabrication step, the diamond membrane is flipped, and another anisotropic O_2 ICP RIE is performed to thin down the membrane to a thickness of $d \approx (1-7)\,\mu\mathrm{m}$.

The edges of the membrane are thereby protected by a quartz mask so that they are not thinned down in order to keep up the sample's structural strength. Here, multiple etching

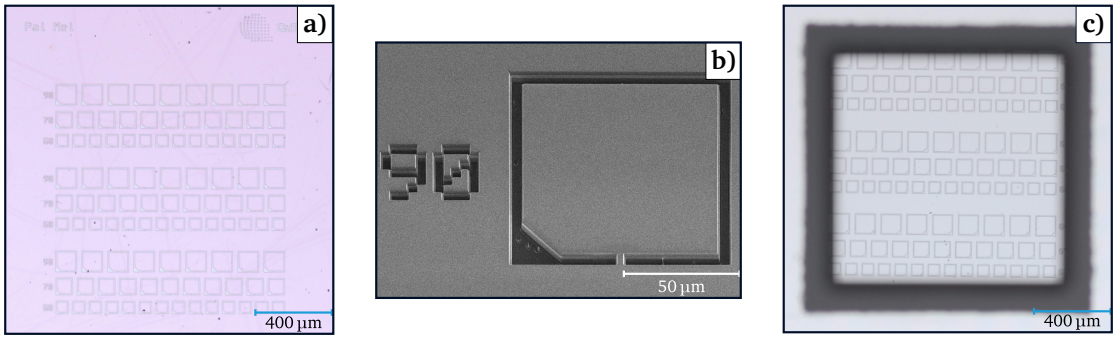

Figure 3.2.3: Microscope pictures after main fabrication steps of the sample *Pai Mei*. **a)** Optical microscope image of the membrane with the platelet trench pattern after CHF_3 etch into the SiN_x layer. **b)** scanning electron microscope (SEM) image of trenches around a future platelet in diamond after the O_2 etch. **c)** Optical microscope image of the flipped diamond membrane with etched trenches on a 4 inch quartz (SiO_2) waver for the Ar/Cl_2 and O_2 backside etch. The square frame on the sides of the image is the quartz mask used to protect the rim of the membrane from etching.

steps with intermediate observations under the optical microscope are used to make sure the platelets are thinned down appropriately. As shown in [7], the height profile after etching is inhomogeneous, with platelets closer to the mask being thicker and platelets in the middle of the membrane being thinner. An Ar/Cl_2 etch of $t = 45$ min is performed before the O_2-etch to prevent micromasking. After this step, the diamond platelets are released from the membrane and only held in place by the $d = (2-5)$ µm thin holding bars (see Fig. 3.2.2 e)). This platelet release backside etch is performed similarly for samples where the trenches are laser cut.

3.2.3 FABRICATION USING LASER CUTTING

Fabricating diamond platelets using e-beam lithography and dry etching is a time-consuming and labor-intensive endeavor. Moreover, the nanometer precision attainable with this method seems unnecessary for the task. In an open microcavity, the optical axis is oriented along the z-direction and can be positioned within the central region of the platelet, micrometers away from the edge. Therefore, we studied an alternative fabrication method that utilizes laser cutting to create trenches.

A protective mask was deposited on top of the membrane to safeguard the diamond membrane's surface from byproduct deposition during laser cutting. Two distinct mask materials were tested on separate samples: a PVA mask and a chromium mask. For the latter, we deposited a chromium layer of $d = 150$ nm using an evaporator (*Temescal, FC-2000 evaporation system*) while the PVA mask was sprayed on. *Lasertec BV* carried out the laser cutting using a femtosecond pulsed laser to achieve $d \approx 15$ nm deep trenches. Following this process, we removed the PVA mask with a $\Delta t_w \approx 10$ min water bath in a sonicator. In contrast, the chromium mask was eliminated by immersing the sample for $\Delta t \approx 15$ min in a chromium etchant (*TechniEtch Cr01*). Subsequently, both samples underwent cleaning using piranha solution and, to eliminate potential graphitizations, a tri-acid cleaning process ($T = 120\,°C$, not boiling). Next, we performed a strain-relief etch, consisting of a single Ar/Cl_2 and one O_2 etch with a total depth of $d \approx 3$ µm, followed by another piranha cleaning. The sample with the PVA mask was then enriched with SnV centers (see Section 3.1.2), while the diamond membrane with the chromium mask had been previously enriched with NV centers. Finally, we executed a backside platelet release etch (see Section 3.2.2).

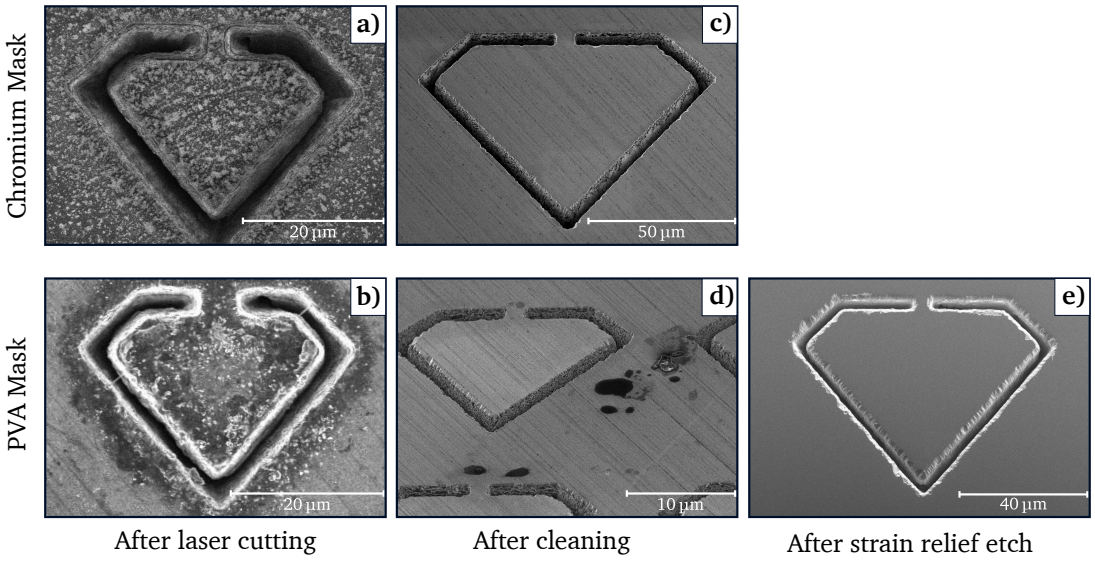

Figure 3.2.4: SEM images of laser-cut diamond membranes with two different surface protection masks after the main fabrication steps. In the first row, pictures of the membrane (*Ringo*) with a chromium mask are shown, while in the second row, pictures of the membrane (*Vincent Vega*) with a poly(vinyl alcohol) (PVA) mask are shown. **a), b)** After laser cutting, but before removal of the mask, a significant amount of dirt is visible. **c), d)** After removing the masks and performing multiple acid cleans, the samples appear to be mostly clean; however, some parts of the sample with the PVA mask remain dirty. Polishing marks are visible on both samples. **e)** An SEM image of the PVA mask sample was taken after the strain relief etch, showing a clean sample and the removal of polishing marks.

EVALUATION OF PROTECTIVE MASKS In Fig. 3.2.4, SEM images of both diamond membranes after laser cutting with the protective mask on, after removal of the mask and acid cleaning, and after the strain relief etch are shown. The significant contamination of the membrane surfaces after laser cutting is clearly visible in Figs. 3.2.4 a) and 3.2.4 b), emphasizing the importance of surface protection masks. After mask removal and acid cleaning, the surfaces of both membranes appear relatively clean in the SEM images (Figs. 3.2.4 c) and 3.2.4 d)). Some residual contamination is visible on the sample with the PVA mask, but its nature could not be further identified. Clear marks, presumably from polishing, are visible on both samples. Only the PVA mask sample was imaged under the SEM again after the strain relief etch (Fig. 3.2.4 e)). In this image, the marks visible before the strain relief etch are no longer apparent. This observation visually complements the measured reduction of surface roughness after the strain relief etch, which was determined using the AFM on a different sample after the interleaving strain relief etch, as shown in Fig. 3.1.1.
In conclusion, both masks appear suitable for protecting the surfaces of diamond membranes during laser cutting. However, the ease of use of PVA as a mask, due to its simple spray-on application and water-soluble removal, makes it preferable over chromium in terms of handling.

CONCLUSION Comparing the laser-cut trenches shown in Fig. 3.2.4 e) with the dry-etched trenches after e-beam lithography visible in Fig. 3.2.3 b) reveals the expected difference in roughness. In contrast, the surface in the middle of the platelet appears unaffected in the SEM images.

3.3 BONDING

3.3.1 PLATELET BONDING

After releasing the platelets, as previously mentioned, they remain held in place by the holding bar. In the final step of fabrication, the platelets are removed from the frame and placed onto a Bragg mirror using a piezo-controlled micromanipulator (*Imina Technologies*) with a needle tip. Proper cleaning and surface activation of both the diamond membrane and the Bragg mirror seem crucial for successful bonding. Consequently, the diamond membrane is carefully cleaned in a HF acid bath. In contrast, the Bragg mirror is cleaned using piranha solution and subsequently exposed to surface activation for $\Delta t_{O3} > 15\,\text{min}$ in a UV-ozone chamber. Following the cleaning process, the diamond membrane is placed on top of a quartz mask with a square opening of $1.4\,\text{mm} \times 1.4\,\text{mm}$, and the quartz mask is positioned on top of the Bragg mirror. Next, the diamond platelets are broken out of the membrane, allowing them to fall onto the mirror by applying pressure from above with the micromanipulator. Once a sufficient number of platelets are positioned on the mirror, the diamond membrane and the quartz mask are removed. If the platelets have not yet bonded, they can be repositioned using the micromanipulator. By applying adequate force on top of the platelets with the micromanipulator tip, bonding was achieved for a significant number of platelets.

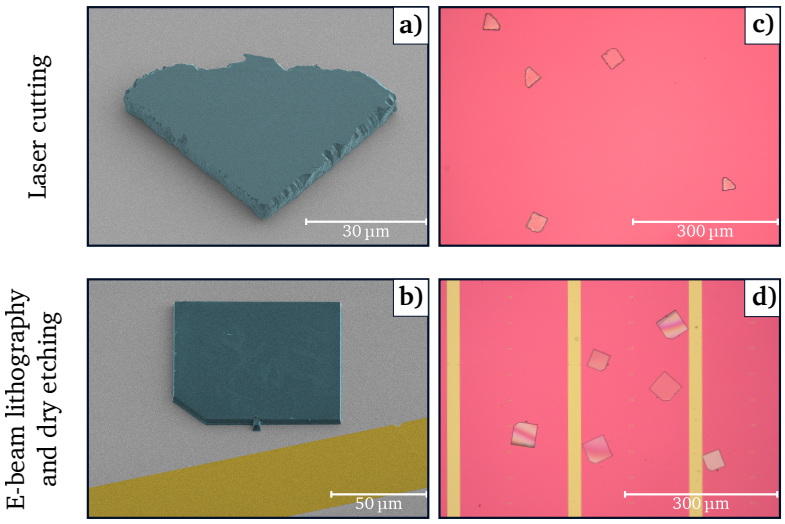

Figure 3.3.1: **a), b)** False-color SEM images of diamond platelets (*blue*) bonded to a Bragg mirror (*gray*). In **b)**, a gold strip line deposited for microwave control of the color centers is displayed in gold. **c), d)** Optical microscope top view images of multiple diamond platelets bonded to a Bragg mirror. In **a)** and **c)**, a tin-implanted platelet from a laser-cut membrane (*Vincent Vega*) is shown, while in **b)** and **d)**, a sample enriched with NV centers fabricated using e-beam lithography and dry etching (*Pai Mei*) is shown.

In this manner, multiple platelets could be bonded to multiple Bragg mirrors for each membrane (see Fig. 3.3.1). This was accomplished using both e-beam lithography and dry etching fabricated samples, as well as laser-cut platelets, indicating that the rough edges of the laser-cut samples did not pose a significant disadvantage in terms of bonding.

3.3.2 PROPOSED METHOD FOR BONDING WITH AN INTERMEDIATE LAYER OF ALUMINA

Bonding a diamond to a Bragg mirror remains challenging, so ways of improving the yield were studied. A proposed method uses a single-digit nanometer-thin intermediate layer of

alumina Al_2O_3 between the bonding surfaces. This was successfully demonstrated on different substrates with a thin deposited alumina layer $d < 3\,\text{nm}$ on both surfaces, using atomic layer deposition (ALD) [40]. As such a layer is way thinner than a quarter wavelength of the used $\lambda = 637\,\text{nm}$, the optical properties in an open microcavity should not be influenced too much. Additionally, the design of the Bragg mirror can be adjusted to compensate for the alumina layer.

The method was tested to bond whole diamond membranes instead of platelets. Therefore, a diamond membrane and a Bragg mirror were piranha cleaned, and a thin layer of alumina was deposited on top $d = 3\,\text{nm}$ of both using ALD (*Oxford instruments, Flexal*). The diamond membrane was put on top of the Bragg mirror directly after taking the sample out of the ALD machine, with the two alumina layers touching. Afterward, pressure was exerted on top of the diamond membrane with tweezers. Finally, an annealing step at $T \approx 300\,°\text{C}$ for $\Delta t \approx 1\,\text{h}$ was performed.

Unfortunately, successful bonding could not be demonstrated for the attempt. However, this could be due to unclean surfaces. Further investigation is necessary to characterize this method better.

3.4 FABRICATION RESULTS

After fabrication, the thickness of the diamond platelets bonded to the mirror was studied using the white light interferometer (WLI), while AFM measurements were performed to characterize the surface roughness.

3.4.1 PLATELET THICKNESS AND SHAPE

In Fig. 3.4.1 a), a height map of a NV center-enriched diamond platelet fabricated by e-beam lithography and dry etching is shown. Here, a clear, close-to-linear height gradient across the diamond platelet between a thickness of $L_{\text{dia}} \approx 4.3\,\mu\text{m}$ and $L_{\text{dia}} \approx 3\,\mu\text{m}$ is visible, as expected. Whether the cavity is in a diamond-like mode or an air-like mode for a given wavelength is only determined by the diamond thickness, as shown in Eqs. (2.3.14) and (2.3.15). In Fig. 3.4.1 a), the positions for possible air-like modes (*green lines*) and possible diamond-like modes (*purple lines*) for the zero-phonon line (ZPL) wavelength $\lambda = 637\,\text{nm}$ of the NV center are shown. As visible, the steep diamond thickness gradient allows for multiple positions where air-like and diamond-like modes are possible. On the one hand, because of impurities or contamination, it is not expected to find good optical properties at all locations on the platelet, which makes the ability to operate in both of these cavity modes in any region of the platelet advantageous. On the other hand, the height gradient of the surface $\Delta L_{\text{dia}}/\Delta d \approx 13\,\text{nm}\,\mu\text{m}^{-1}$ introduces a deviation from the one-dimensional cavity theory. Because the Gaussian beam waist at the platelet surface is in the order of $1.5\,\mu\text{m}$, the diamond thickness L_{dia} differs substantially across it, which alters the electric field distribution inside the cavity and can introduce further unwanted cavity losses.

In Fig. 3.4.1 b), a three-dimensional view of the same diamond platelet is shown with a gold strip line next to it.

WLI imagery of a laser-cut diamond platelet bonded to a Bragg mirror, as displayed in Fig. 3.4.2 a), shows not only a thickness gradient across the platelet but also a gradient

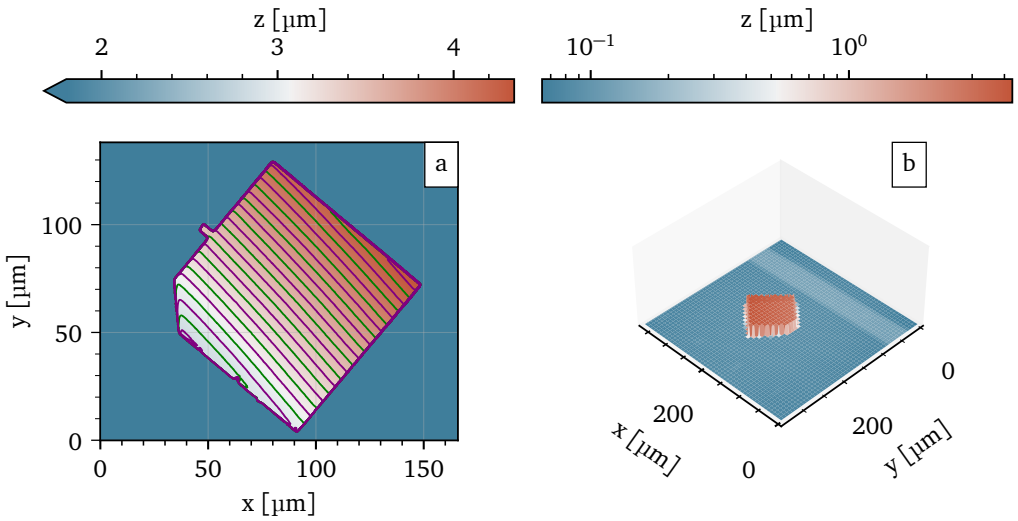

Figure 3.4.1: **a)** Height map of an NV center-enriched, e-beam lithography and dry etching fabricated diamond platelet (*Pai Mei*) bonded to a Bragg mirror. The data was acquired using a WLI. The *green lines* show possible air-like modes by forming a cavity at the corresponding positions, while the *purple lines* show the possible diamond-like mode positions. A clear height gradient is visible across the platelet, leading to multiple contour lines where diamond-like and air-like modes are possible. **b)** Three-dimensional plot of the height data of the same platelet as shown in a) with a logarithmic colormap. Here, the height gradient is also visible, as well as the gold strip line next to the platelet.

towards the platelet edges, where the diamond gets thinner. Additionally, a trench-like pattern is observable at the platelet edges. This effect is only visible on the top side of the platelets and can only be observed with the WLI if the diamond platelet did not flip during the bonding process. In comparison, in Fig. 3.4.2 b), a platelet is shown that flipped during the bonding process, so the side exposed to the backside platelet release etch faces up. Here, the area at the edges is more uniform.

A reason for this tapering of the edges most likely lies in the etching behavior of the backside etch at the point where the trenches are already etched through. Because the trenches of the laser-cut samples are with $d \approx (10-15)\,\mu\text{m}$, far deeper than the aimed final thickness of the platelet, etching needs to continue after this point for a longer time in comparison to the e-beam lithography and dry etching fabricated samples. This enables the O_2 plasma, which is not perfectly directional, to access those areas on the top side of the platelets for a substantial amount of time. The trench-like pattern at the edge could be caused by transferred irregularities from the edges of the platelet due to the laser-cutting (cf. Fig. 3.2.4 e)).

These tapered edges make this platelet region unsuitable for use in the open microcavity due to the expected insufficient optical properties. For larger platelets, such as the $70\,\mu\text{m} \times 70\,\mu\text{m}$ platelets shown in Fig. 3.4.2, this is not a major issue due to the sufficiently large usable area in the middle of the platelet. However, this effect leads to a small or no usable area for smaller platelets. A future laser-cut design should aim for shallower trenches and sufficiently large platelets to reduce the effect.

3.4.2 SURFACE ROUGHNESS AND WAVINESS

A smooth surface is not just important for bonding but also for minimizing scattering losses at the diamond surface in the cavity [32, 41]. While for bonding, strong height variations

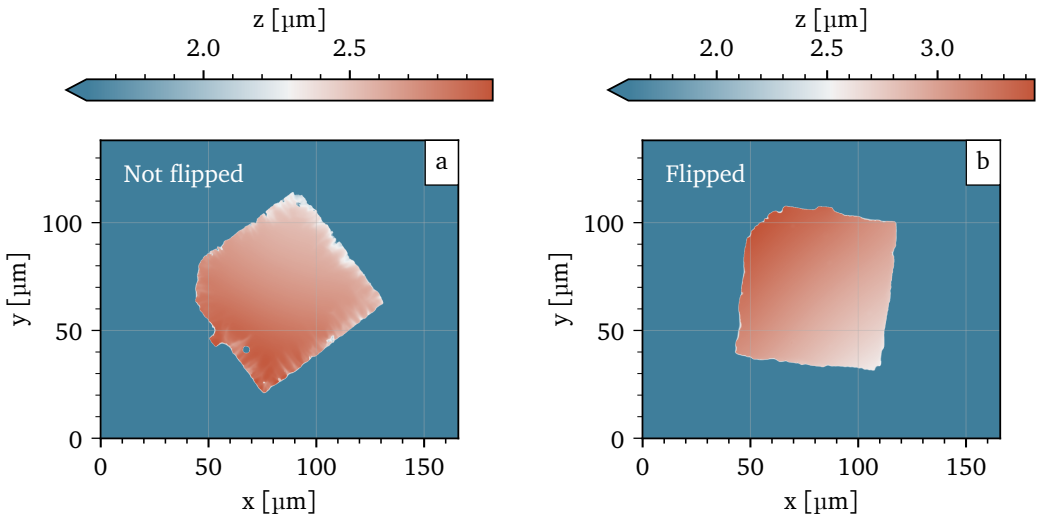

Figure 3.4.2: Height map of two different diamond platelets from the same laser-cut diamond membrane (*Vincent Vega*), measured using a WLI. **a)** This platelet did not flip during the bonding procedure. A clear trench-like pattern and tapering is observable on the edges of the platelet, presumably caused by O_2 plasma having access to the area etching during the backside etch. **b)** This diamond platelet did flip, so the visible side was exposed to the backside etch. Here, the edges are more uniform.

over multiple micrometers seem to be problematic because they can prevent large areas of the surface from being close to the mirror, for low scattering losses, the surface needs to be smooth in the Gaussian mode beam waste $\omega_0 \approx 1.5\,\mu\text{m}$ area. To make this distinction, the height data is decomposed into high-frequency and low-frequency components referred to as roughness and waviness respectively [42]. This is achieved by Fourier transforming the height data and removing the high-frequency components ($f > 2\,\mu\text{m}^{-1}$). Applying the inverse Fourier transform results in the data for the waviness. The waviness is subtracted from the measurement data to get the roughness, which removes the low-frequency components. The RMS roughness or waviness parameter R_q and W_q are then calculated by

$$\rho_\text{q} = \sqrt{\frac{1}{N}\sum_{i=1}^{N} |z_i - z_\text{mean}|^2}, \tag{3.4.1}$$

where z_mean is the average height, z_i the measured points and N the number of measured points.

In Fig. 3.4.3, the analyzed AFM data from the not-flipped laser-cut diamond platelet discussed in the previous section is shown (*Vincent Vega*). The surface roughness $R_\text{q} \approx 0.8\,\mu\text{m}$ on this platelet is significantly higher than on other samples (cf. Fig. 3.1.1 b)). One reason could be the exposure to the O_2 plasma during the backside etch, as described in the previous section, as a possible reason for the tapered edges and the trench-like structures on the platelet. In this configuration, with the relevant area being only through the trenches exposed to the plasma, a homogeneous etch behavior is not expected, which could increase surface roughness and waviness. Further measurements are needed to verify this effect. Another explanation could be the shallow strain relief etch performed on the platelet, which was aimed to remove only $d \approx 3\,\text{nm}$ of the surface.

AFM measurements were also performed on the flipped platelet introduced in the previous section. Here, a significantly lower surface roughness with $R_\text{q} \approx 0.3\,\text{nm}$ but a approximately

similar waviness $W_q \approx 0.5\,\text{nm}$ was measured.

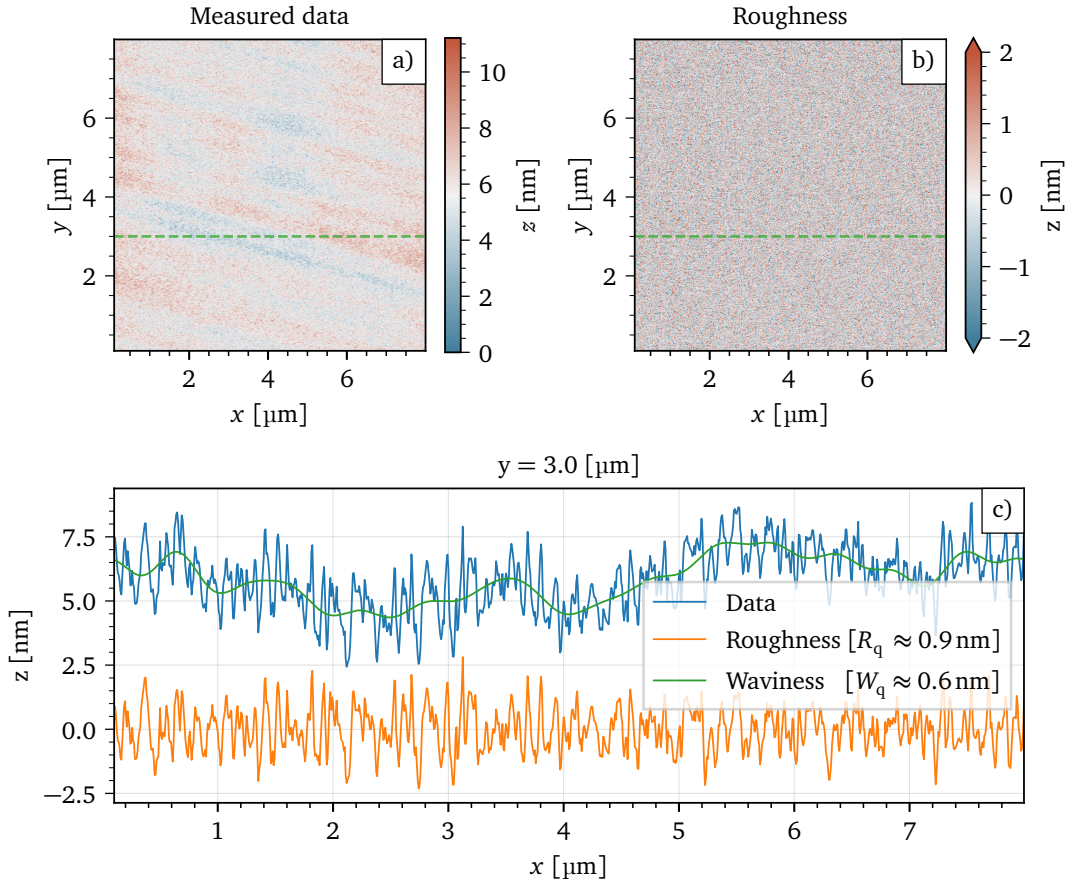

Figure 3.4.3: Analyzed height data from an AFM measurement on a laser-cut diamond platelet bond to a Bragg mirror, which did not flip during bonding (*Vincent Vega*). **a)** The measured height data shows a stripe-like waviness. **b)** Here, only the high-frequency components of the surface ($f > 2\,\mu\text{m}^{-1}$) are shown, namely the roughness. The determined RMS roughness parameter of $R_q \approx 0.8\,\text{nm}$ is significantly higher then achieved on other samples (cf. Fig. 3.1.1 b)). In **c)**, a single line of the AFM measurement, corresponding to the *dotted green lines* in a) and b) is shown to illustrate the difference between roughness and waviness. In *blue*, the measured height data is displayed, while the *green* line shows the waviness, where the high-frequency components ($f > 2\,\mu\text{m}^{-1}$) are removed. In orange, the roughness is shown, where the waviness was subtracted at every data point.

4 | CHARACTERIZATION OF EMITTER PROPERTIES

Good optical properties of the color centers in the fabricated diamond platelets are key for usage in future quantum information experiments. Especially, spectrally stable and narrow emission lines are important to ensure the indistinguishability of emitted photons necessary for entanglement generation by two-photon quantum interference as shown in [43]. In this chapter, the methods used to characterize optical properties of the nitrogen-vacancy (NV) and tin-vacancy (SnV) center are outlined, followed by a discussion of the acquired measurement results.

4.1 CONFOCAL MICROSCOPY AT CRYOGENIC TEMPERATURES

4.1.1 EXPERIMENTAL SETUP

To characterize the emitter properties of the SnV and NV centers in the fabricated diamond platelets bond to a Bragg mirror, a home-built confocal microscopy setup is used. The sample is placed in a closed-cycle cryostat (*Montana Instruments s50*) to maintain temperatures below ($T < 10\,\mathrm{K}$).

EXCITATION PATH For off-resonant excitation of the emitters, a green laser (*Hübner Photonics, Cobolt 06-MLD*) at $\lambda = 515\,\mathrm{nm}$ is used. For resonant excitation of the SnV center, a red laser at $\lambda = 619\,\mathrm{nm}$ (*Toptica TA-SHG pro*) is used, while a red laser at $\lambda = 637\,\mathrm{nm}$ (*New Focus Velocity TLB-6700*) is used for resonant excitation of the NV center (see Fig. 4.1.1 a) *yellow*). The two red lasers used for resonant excitation are frequency locked to a wavemeter (*HighFinesse WS-6*) via a PC-controlled proportional–integral–derivative (PID) loop acting on the laser control. A fiber-based acousto-optic modulator (AOM) controlled by the ADwin (*Jaeger ADwin Pro II*) is used to shape µs-pulses for those lasers. The pulses of the green laser are shaped by the ADwin acting directly on the laser control. Subsequently, the lasers are combined using a free-space dichroic beam splitter (BS) and again coupled to an optical fiber.

CONFOCAL MICROSCOPY The light is focused onto and collected from the sample using an *Olympus MPLFLN-100X* microscope objective mounted on a homebuilt piezo xyz-stage (*Physik Instrumente P-615K011*). In combination with a camera setup (Fig. 4.1.1 c) *blue*), an optical microscope is formed to localize features and navigate on the sample.

DETECTION PATH In the detection path (Fig. 4.1.1 b), *green*), the resonant and off-resonant excitation lasers are optically filtered out, and only the phonon sideband (PSB) light of the

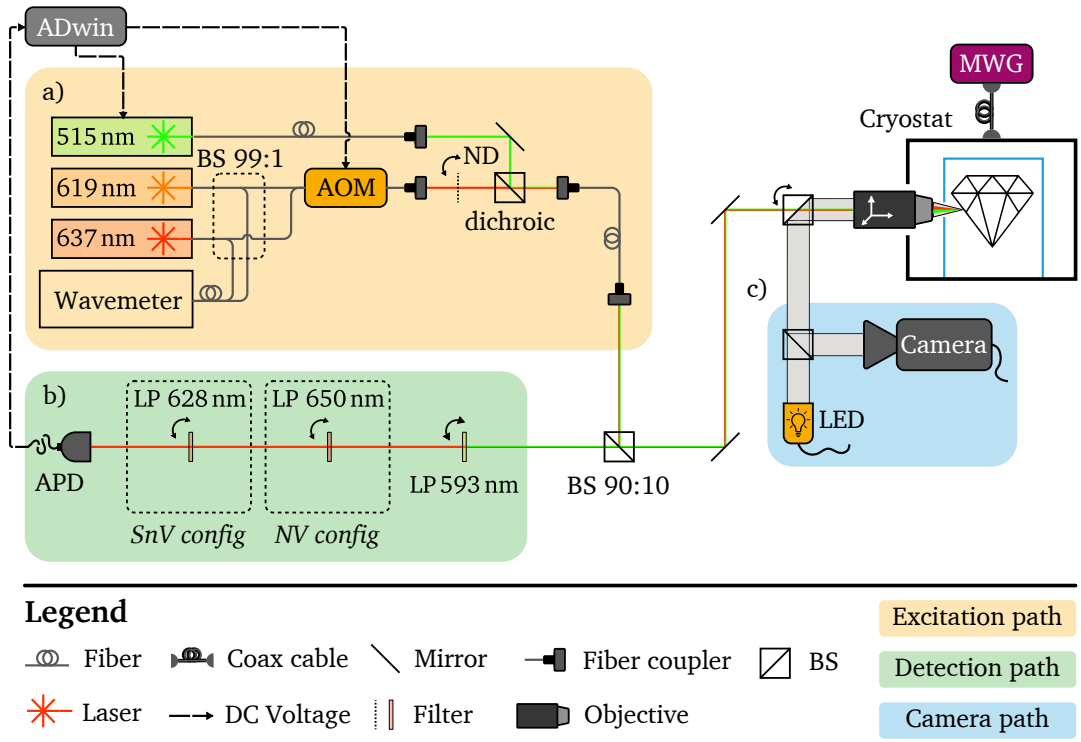

Figure 4.1.1: Schematic overview of the experimental setup used for emitter characterization.**a)** The yellow part shows the excitation path, while in the green part **(b)**, the detection path is shown. **c)** In the blue marked part, the camera setup to see a microscope image of the sample is displayed. All non-labeled beam splitters have a reflection of 50:50, and the unwanted light leakage is not displayed in the graphic. The used abbreviations are: AOM: acousto-optic modulator, BS: beam splitter, LP: longpass Filter, SP: shortpass Filter, ND: neutral density Filter, APD: avalanche photodiode, MWG: microwave generator.

emitter is collected. The green laser light is filtered out by a longpass (LP) filter with an edge at 593 nm (*Thorlabs, FELH0600*), while different additional LP filters are used for filtering out the resonant lasers for the SnV (LP 628 nm, *Semrock, TLP01-628*) and NV center (LP 650 nm, *Semrock, BLP01-633R*) studies (see Fig. 4.1.1 b) *dotted boxes*). The filtered light is coupled to an optical fiber and detected by an avalanche photodiode (APD) (*Laser Components, COUNT*), which is connected to a counter module of the ADwin.

MICROWAVE To supply the sample with microwaves, a microwave generator (MWG) (*Rhode and Schwarz, sgs100a*) is connected to the cryostat input lines, which in turn are connected to the printed circuit board (PCB) on which the sample is mounted. There, connection lines are wire-bonded to the golden strip lines on the mirror, which are tens of micrometers away from the diamond platelets (see Fig. 3.3.1 d)).

4.1.2 PHOTOLUMINESCENCE EXCITATION (PLE)

To measure the dephasing and spectral diffusion linewidth of the color centers, photoluminescence excitation (PLE) scans are performed. Here, a laser is scanned in frequency over the optical resonances of the emitter, and the emitted fluorescence is collected.

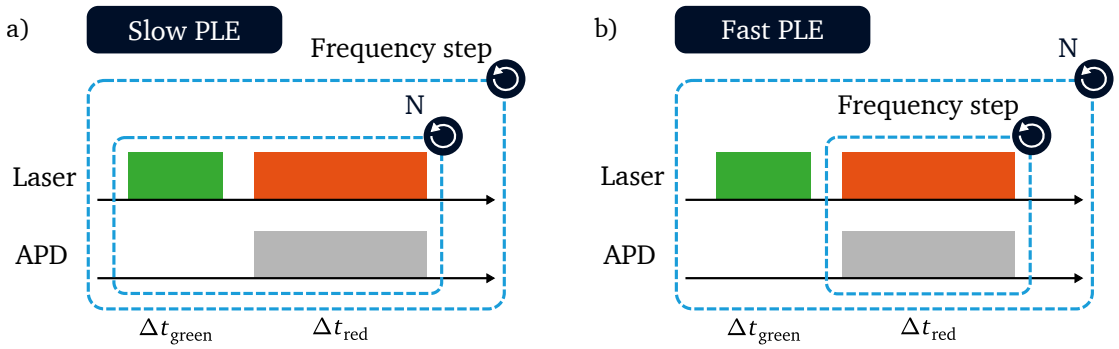

Figure 4.1.2: Pulse sequences of slow and fast PLE scans. **a)** For the slow PLE scans, at every frequency step N, interleaved green and red pulses are sent until the integration time is reached. **b)** For the fast PLE scans, after an initial green pulse, a single red pulse is sent at every frequency step. This procedure is repeated N times to build up statistics.

SLOW PLE

Two types of PLE scans are used throughout this thesis. To scan a large frequency range slow PLE scans are used (see Fig. 4.1.2 a)), where at every frequency step first a green laser pulse with power P_{green} is applied for the time Δt_{green} to ensure that the emitter is in the correct charge state and to counteract optical spin pumping. Then, a red laser pulse with power P_{red} is applied for Δt_{red} while the emission is detected via the APD. Those two pulses are interleaved at every frequency step until the integration time Δt_{int} is reached. The frequency of the red laser is locked to the wavemeter and swept by adjusting the locking set frequency. Using this method, the charge environment, and therefore the resonance frequency of the emitter, changes while scanning over it because of the slow frequency scanning speed and the interleaved green pulses. Therefore, the dephasing linewidth is always superimposed by the spectral diffusion linewidth, making it impossible to measure the dephasing linewidth.

FAST PLE

To measure the dephasing linewidth, a different kind of PLE scan is needed, with a faster scanning speed and without interleaved green pulses which lead to changes in the charge environment. For this fast PLE scans (see Fig. 4.1.2 b)), only one green laser pulse with power P_{green} and duration Δt_{green} at the beginning of the sequence is used to ensure the correct charge state of the emitter. Afterward, the frequency is swept. At every frequency step, only a red pulse for time Δt_{red} and with power P_{red} is used while emitted photons are detected using the APD. To be able to sweep the frequency of the laser in this fast manner, the laser control voltage is directly manipulated instead of using the PID locking. Without locking the laser, long scans over a large frequency range are not reliably possible because frequency drifting of the laser can occur, as well as mode hopping.

FAST PLE ON NV CENTER In fast PLE scans without microwave driving, it is difficult to measure transition lines due to rapid spin pumping, which prevents further optical driving. For slow PLE scans, this is not a major issue because the interleaved green laser pulses populate both ground states again [24]. For the SnV center, the population decays from the lower branch of the excited state into both ground states. Due to phonon-mediated transitions [28, 44] between the two ground states, the population does not end up in an optically dark state, making fast PLE scans possible.

4.1.3 OPTICALLY DETECTED MAGNETIC RESONANCE (ODMR) OF THE NV CENTER

For optically detected magnetic resonance (ODMR) spectroscopy, the NV center is continuously off-resonantly excited using the green laser, while the MWG is used to sweep the microwave frequency across the resonance frequency of the $^3A_2$ ground state splitting. The emitted fluorescence is collected by the APD. If the microwave frequency is resonant with the ground state energy splitting, transitions between the $m_s = 0$ and $m_s = \pm 1$ states are driven. Due to the lower photoluminescence of the $m_s = \pm 1$ states compared to the $m_s = 0$ state when excited, the overall detected counts on the APD decrease, leading to a dip in the acquired microwave spectrum.

By employing this method, the ground state energy splitting of the NV center can be measured. This information can be utilized to resonantly microwave drive the ground state transitions during PLE measurements, making the transitions between the $m_s = \pm 1$ ground and excited states (^3E) visible. As previously discussed, this also enables the acquisition of fast PLE spectra of the NV center.

4.2 MEASUREMENT RESULTS

4.2.1 SnV CENTERS IN DIAMOND PLATELETS

To characterize the optical properties of the SnV centers in the fabricated samples at $T < 10\,\mathrm{K}$, the confocal microscope setup is used. The characterized diamond platelet was fabricated using the laser cut method. In the first step, emitters are localized by a two-dimensional confocal scan over the diamond platelet. Therefore, the emitters are off resonantly excited with the green laser ($P_{\mathrm{green}} \approx 500\,\mu\mathrm{W}$), and the emission is detected by the APD.

In Fig. 4.2.1 a), a confocal map covering the whole platelet made in a room temperature setup is shown. There is no emitter emission detectable at the edge of the sample. This is due to the undesired removal of several tens of nanometers of diamond around the edge, including the shallow implanted SnVs, which was observed using the white light interferometer (WLI) (see Section 3.4.1). Near the end of the backside etch, when the trenches are already etched through, the O_2-plasma has access to those positions, which could be the reason for the removal of material. The deeper trenches $d = (10 - 15)\,\mu\mathrm{m}$ of the laser-cut sample can be attributed to this effect.

Furthermore, fast PLE scans are used to measure the linewidth of single emitters (Fig. 4.2.1a),b) and Fig. 4.2.2). On every emitter position $N = 100$ of those scans are performed ($P_{515} = 1\,\mu\mathrm{W}$, $P_{619} = 0.1\,\mathrm{nW}$). Empty traces, which are included in Fig. 4.2.2 a), are caused by ionization of the SnV and are excluded from the analysis. Since before every fast scan, a green laser pulse is applied ($\Delta t_{515} = 100\,\mathrm{ms}$, $P_{515} = 1\,\mu\mathrm{W}$), the charge environment of the emitter can change, which leads to spectral diffusion (see Fig. 4.2.2 a)). In Fig. 4.2.2 c) (*Orange crosses*) the summed up counts of Fig. 4.2.2 b) are displayed. The spectral diffusion linewidth is then gathered by fitting a Gaussian. The narrowest observed spectral diffusion linewidth (full width at half maximum (FWHM)) is $\Gamma_s = 58.3(21)\,\mathrm{MHz}$.
To gather the dephasing linewidth, the single PLE traces are fitted by a Lorentzian and centered using the center frequency of the Lorentzian, as shown in Fig. 4.2.2 b). Afterward, the centered traces are summed and again fitted by a Lorentzian (see Figs. 4.2.1 c) and 4.2.2 c) (Blue circles)). The narrowest observed dephasing linewidth is $\Gamma_d \approx 32.5(4)\,\mathrm{MHz}$, which is close to the lifetime limited linewidth (for $\tau \approx 6\,\mathrm{ns} \rightarrow \Gamma_0 = (2\pi \cdot \tau)^{-1} = 26.5\,\mathrm{MHz}$) of the SnV reported in literature [6].

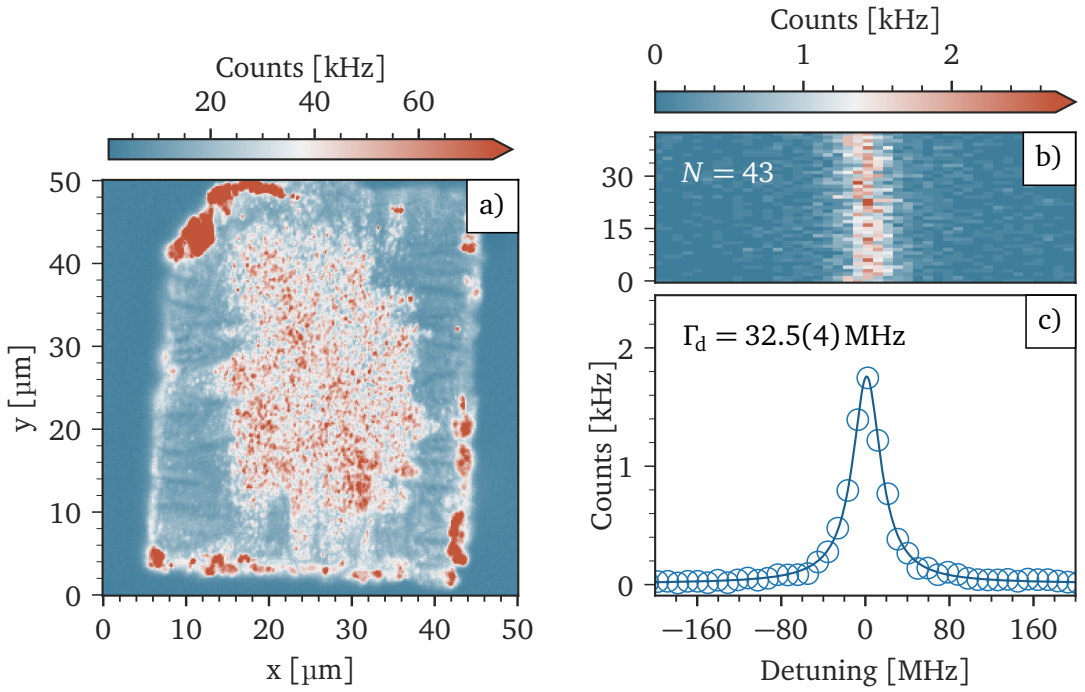

Figure 4.2.1: **a)** Confocal map of laser cut diamond platelet with implanted SnV centers bond to a mirror (*Vincent Vega*). The outline of the platelet is clearly visible, as well as the SnV centers in the middle of the platelet. **b)** PLE scan result of a SnV, centered and without empty traces. The experimental parameters are: $P_{\text{green}} \approx 1\,\mu\text{W}$ $\Delta t_{\text{green}} = 100\,\text{ms}$, $P_{\text{red}} \approx 0.2\,\text{nW}$, $\Delta t_{\text{red}} = 10\,\text{ms}$, $N = 100$. **c)** Summed up traces from b) with fitted Lorentzian showing a dephasing linewidth of $\Gamma_{\text{d}} = 32.5(4)\,\text{MHz}$.

CONCLUSION For future entanglement experiments between two SnV centers, the emitted photons need to be indistinguishable in frequency, requiring a narrow dephasing linewidth ($\Gamma_{\text{d}} < 100\,\text{MHz}$ [18]). A narrow spectral diffusion linewidth allows for a higher success rate in a charge-resonance-check and therefore leads to a higher entanglement rate [17]. Although the narrowest dephasing linewidth and the narrowest spectral diffusion linewidth were measured for different SnV centers, there is no inherent reason why further studies of the sample should not reveal SnV centers possessing both qualities.

4.2.2 NV CENTERS IN DIAMOND PLATELETS

Also, a NV center-enriched diamond platelet sample (*Mr. Orange*) bond to a Bragg mirror was studied in the confocal setup. The studied platelets did not properly bond to the Bragg mirror, most likely due to a large amount of surface contamination. It must therefore also be assumed that the optical properties of that sample in an open microcavity would be insufficient. But, because these factors should not significantly impact the optical linewidth of the NV centers, the inside gathered with measurements of the emitters can be used as a benchmark for similar samples. However, bonding could alter the strain inside the diamond at cryogenic temperatures, among others, due to the different thermal expansion coefficients of the mirror and the diamond [18].

Here, following the same procedure used for the SnV center-enriched sample, emitters are first localized by performing a two-dimensional confocal scan over the diamond platelet. The microscope is then focused on a potential NV center position, and slow PLE scans are conducted. Due to the absence of gold strip lines on the mirror, no microwaves could be supplied to the NV centers, and therefore fast PLE measurements were not performed. Con-

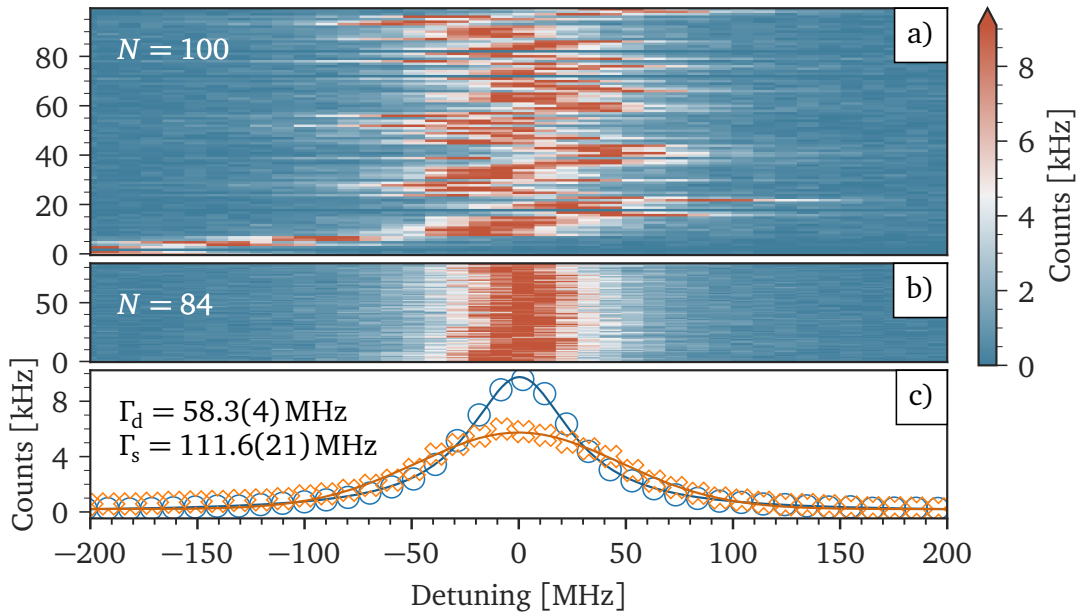

Figure 4.2.2: Fast PLE scan of a second SnV in a laser cut diamond platelet bond to a mirror (*Vincent Vega*). The experimental parameters are: $P_{\text{green}} \approx 1\,\mu\text{W}$ $\Delta t_{\text{green}} = 100\,\text{ms}$, $P_{\text{red}} \approx 0.2\,\text{nW}$, $\Delta t_{\text{red}} = 10\,\text{ms}$. **a)** $N = 100$ PLE scans, containing some partially empty traces due to ionization of the SnV center as well as visible spectral jumps due to the green repump pulses. **b)** Centering of non-empty traces for evaluation of the dephasing linewidth. **d)** (*Blue circles*) Summed up traces from b) with fitted Lorentzian showing a dephasing linewidth of $\Gamma_{\text{d}} = 58.3(4)\,\text{MHz}$. (*Orange crosses*) Summed up traces from a) after removing empty traces, with fitted Gaussian showing a spectral diffusion linewidth of $\Gamma_{\text{s}} = 111.6(21)\,\text{MHz}$.

sequently, only the spectral diffusion linewidth could be measured.

In Fig. 4.2.3 c), an emission spectrum obtained using slow PLE is displayed, showing two visible transition peaks. Assuming they belong to the same NV center, these peaks can be attributed to emissions from the E_{x} (*left*) and E_{y} (*right*) excited states. Since the population is predominantly in the $m_{\text{s}} = 0$ state without microwave driving of the ground state splitting, other transitions are not visible. It is important to note that the assumption that these peaks originate from the same NV center cannot be made with certainty; shifted transitions due to, for example, different strains of two NV centers seem equally likely.

A Voigt function was fitted to the emission peaks (Figs. 4.2.3 a) and 4.2.3 b)), yielding spectral diffusion linewidths of $\Gamma_{\text{s}}^{a} \approx 71.3(5)\,\text{MHz}$ and $\Gamma_{\text{s}}^{b} \approx 55.2(2)\,\text{MHz}$. Even the measured spectral diffusion linewidths, which must be larger than the dephasing linewidth, are narrower than the mentioned estimated maximum dephasing linewidth of $\Gamma_{\text{d}} < 100\,\text{MHz}$ [18], relevant for achieving indistinguishability of emitted photons from multiple NVs. This makes them potentially suitable for entanglement experiments.

A laser-cut diamond platelet containing NV centers (*Ringo*) was also studied at low temperatures. The narrow spectral diffusion linewidths, shown in Fig. 4.2.3 a), could not be replicated when measuring this sample. The observed broadened lines could be a consequence of the laser cutting, although an obvious mechanism explaining this, apart from introduced damage to the crystal structure, could not be found. For a definite conclusion, further measurements are needed, for example, Raman spectroscopy, to quantify damages to the crystal

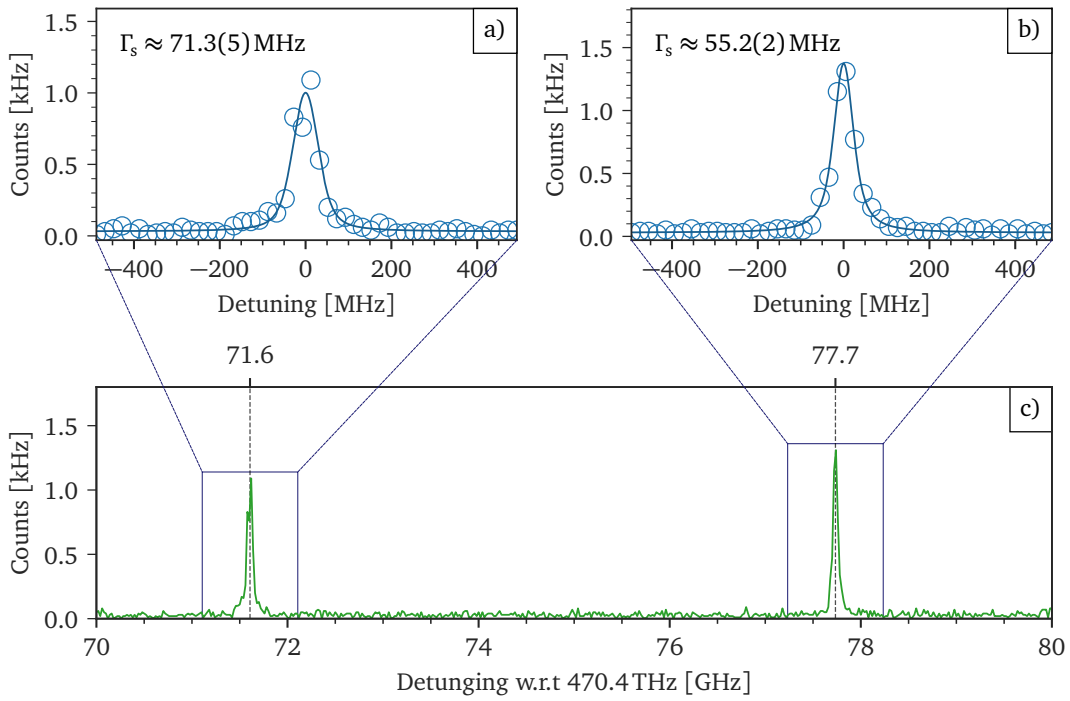

Figure 4.2.3: Emission spectrum of an NV center in a diamond platelet (*Mr. Orange*) fabricated using electron beam (e-beam) lithography and dry etching, bonded to a Bragg mirror, as measured by slow PLE ($P_{515} \approx 40\,\mu$W, $P_{637} \approx 40\,$nW, $\Delta t_{\text{int}} = 100\,$ms). In **c)**, the total measured spectrum is displayed with resonant peaks indicated. **a)** and **b)** provide zoomed-in views of the resonant peaks, plotted as blue circles and fitted to a Voigt function (*blue line*). The spectral diffusion linewidths of the transitions are approximately $\Gamma_s^a \approx 71.3(5)$ MHz and $\Gamma_s^b \approx 55.2(2)$ MHz.

structure [45].

Although the optical properties of the sample are not sufficient, an ODMR measurement was performed (see Fig. 4.2.4 c)), to show the ability to supply microwaves to the sample using the deposited gold strip lines on the mirror. This ability is important for achieving full spin control over NV centers in the fabricated sample, which is a key requirement for using the system as a quantum network node.

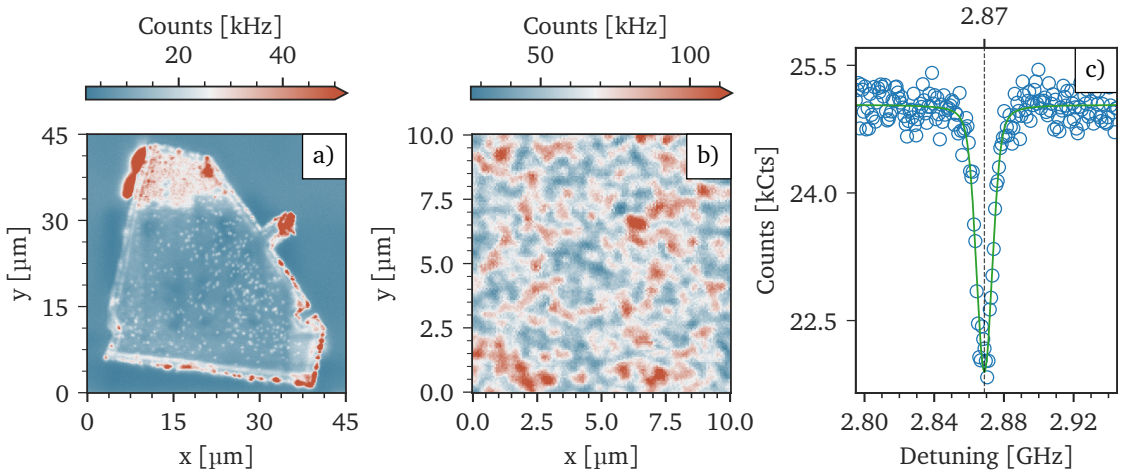

Figure 4.2.4: **a)** Confocal map over the entire diamond-shaped platelet (*Mr Orange*, same sample as in Fig. 4.2.3). In the middle of the platelet, emitters are visible (*white dots*), while especially on the edges of the platelet, other emission sources are present, presumably from contamination. **b)** Confocal map on the laser-cut platelet (*Ringo*). The NV density appears higher than in the platelet shown in a), although the electron dose ($D_{e^-} \approx 4 \cdot 10^{13}\,\mathrm{e/cm^2}$) and thicknesses ($d \approx 3(1)\,\mu\mathrm{m}$) are similar, suggesting that the nitrogen concentration could differ across these diamonds. **c)** ODMR spectrum of the laser-cut sample (*Ringo*) at room temperature. This demonstrates that the fabricated gold strip lines on the mirror are capable of delivering microwaves to the NV centers in the platelet, which is an important first step for achieving full spin control.

4.3 CONCLUSION

It could be demonstrated that the SnV centers and NV centers in the fabricated diamond platelets possess narrow linewidths (SnV: $\Gamma_d^{\mathrm{min}} = 32.5(4)\,\mathrm{MHz}$, NV: $\Gamma_s^{\mathrm{min}} = 55.3(2)\,\mathrm{MHz}$), fulfilling a key requirement for entanglement generation between two color centers. For SnV centers, this was shown using laser-cut samples, while for NV samples, this could only be demonstrated for samples fabricated using e-beam lithography and dry etching. An acquired ODMR spectrum demonstrates the ability to drive the ground state transitions, which is a first step toward achieving full spin control of the system.

5 | CHARACTERIZATION IN AN OPEN MICROCAVITY SETUP

Apart from good optical emitter properties, the diamond platelets should also introduce as few losses as possible when used in an open microcavity. As discussed in Section 2.2, the Purcell factor is directly proportional to the finesse $\mathscr{F}$, while the finesse $\mathscr{F} = 2\pi/\mathscr{L}$ is inversely proportional to the cavity losses. Therefore, the measured finesse of the hybrid-cavity can, on the one hand, gives an estimation of the achievable Purcell factor and, therefore, the branching ratio into the zero-phonon line (ZPL), and on the other hand, by comparing it to the finesse on a bare mirror, shows the amount of cavity losses introduced by the diamond platelets.

In this chapter, the measurement methods to determine the finesse, the air gap, and the diamond thickness of the formed hybrid cavity are shown, and the results are discussed. Finally, an estimation of the achievable Purcell factor and branching ratio into the cavity mode β_{cav} for the nitrogen-vacancy (NV) center and tin-vacancy (SnV) center emission in the fabricated diamond platelet samples using the optical microcavity setup is made.

5.1 METHODS

The characterization measurements were performed in a room-temperature fiber-based open microcavity. Fundamentally, in such a system, the cavity is formed by a Bragg mirror which is deposited on the tip of an optical fiber, and the plane Bragg mirror, where the diamond platelets are bonded to, as shown in Fig. 5.1.1 d). The light is coupled into the cavity, coming from the laser preparation setup through the optical fiber. The transmitted light is collected through the backside of the plane mirror by an objective and guided to the detection path.

5.1.1 OPTICAL FIBER TIP AND PLANE MIRROR

A spherical dimple is fabricated into the fiber by CO_2-laser ablation (*performed by Martin Eschen from TNO Delft*). This is necessary to minimize lateral cavity losses and achieve a stable cavity arrangement. Afterward, the fiber tip is coated with alternating layers of silicon dioxide (SiO_2) and tantalum pentoxide (Ta_2O_5) to create a Bragg mirror. The mirror acts as an optical band-stop filter, which is designed to be highly reflective in the range of $(600-680)\,\text{nm}$, with the lowest transmission of $\mathscr{L}_{\text{fm}}(\lambda = 637\,\text{nm}) \approx 50\,\text{ppm}$ at the ZPL frequency of the NV center. For the ZPL frequency of the SnV center, a higher transmission of $\mathscr{L}_{\text{fm}}(\lambda = 619\,\text{nm}) \approx 80\,\text{ppm}$ is specified.

The plane mirror is fabricated by depositing a similar Bragg mirror to a 4-inch SiO_2 waver, which is then cut into $1\,\text{cm} \times 1\,\text{cm}$ squares. This mirror's reflectivity is lower by design

to achieve a higher outcoupling towards the detection path. The transmission at the subsequent wavelengths in a bare cavity is specified as $\mathscr{L}_{\mathrm{pm,bc}}(\lambda = 637\,\mathrm{nm}) \approx 280\,\mathrm{ppm}$ and $\mathscr{L}_{\mathrm{pm,bc}}(\lambda = 619\,\mathrm{nm}) \approx 915\,\mathrm{ppm}$. The transmission through the plane mirror is higher for the hybrid cavity due to the termination of the high-reflective-index material diamond $n_{\mathrm{dia}} \approx 2.4$ instead of air $n_{\mathrm{air}} \approx 1$. Here the transmission is specified as $\mathscr{L}_{\mathrm{pm,hc}}(\lambda = 637\,\mathrm{nm}) \approx 700\,\mathrm{ppm}$ and $\mathscr{L}_{\mathrm{pm,hc}}(\lambda = 619\,\mathrm{nm}) \approx 1995\,\mathrm{ppm}$. All coatings are applied and characterized by *Laseroptik*.

5.1.2 EXPERIMENTAL SETUP

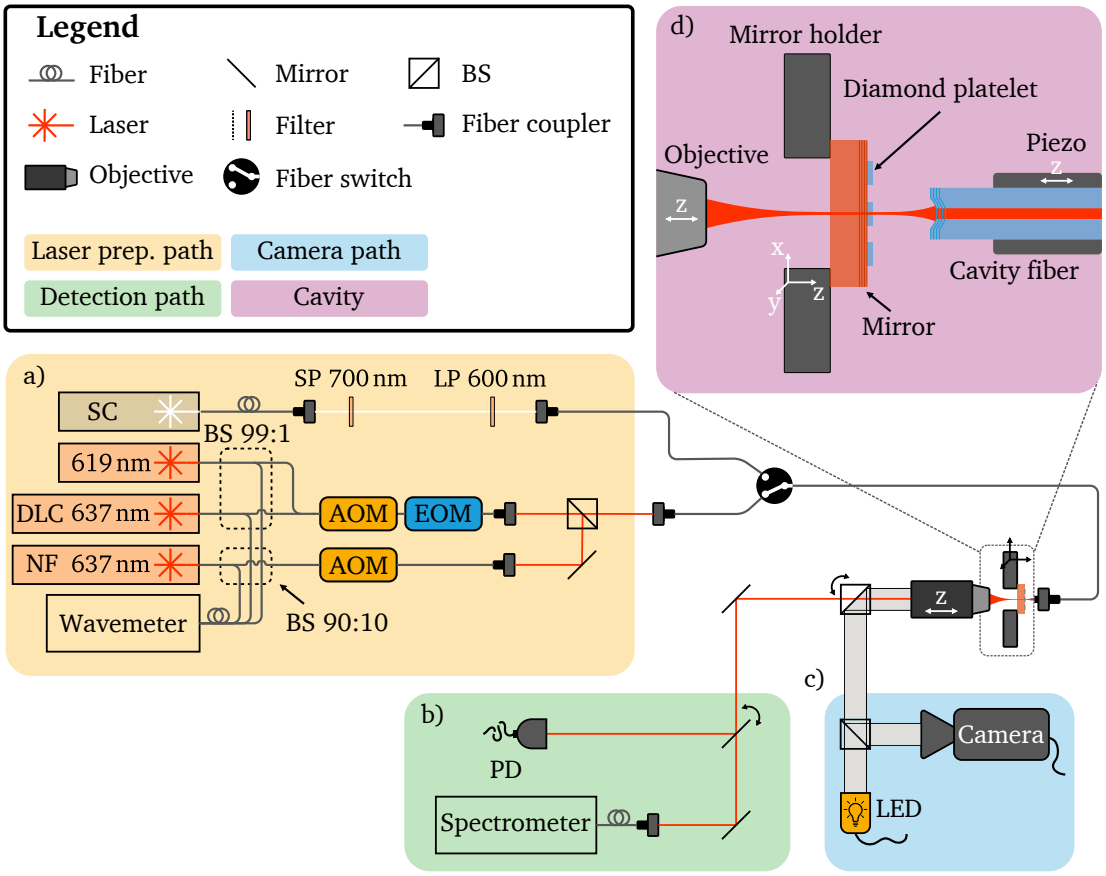

Figure 5.1.1: Schematic overview of the room temperature cavity setup.**a)** The yellow part shows the laser preparation path, while the detection path is shown in the green part **b)**. **c)** In the blue marked part, the camera setup to see a microscope image of the sample, and the fiber tip is displayed. **d)** The purple region shows a zoomed-in view of the cavity. All non-labeled beam splitters have a reflection of 50:50, and the unwanted light leakage is not displayed in the graphic. The used abbreviations are: AOM: acousto-optic modulator, EOM: electro-optic modulator BS: beam splitter, LP: longpass Filter, SP: shortpass Filter, APD: avalanche photodiode.

LASER PREPARATION PATH Four different fiber-coupled lasers are used for the characterization (see Fig. 5.1.1 a)). For measuring the cavity length (see Section 5.1.3), a pulsed supercontinuum laser ($\lambda = 450\,\mathrm{nm} - 2\,\mu\mathrm{m}$, *NKT Femptopower supercontinuum laser*) is utilized. A shortpass (SP) (*Thorlabs, FELSH700*) and a longpass (LP) (*Thorlabs, FELH600*) filter at $\lambda_{\mathrm{SP}} = 700\,\mathrm{nm}$ and $\lambda_{\mathrm{LP}} = 600\,\mathrm{nm}$ reduce the optical bandwidth of the laser light, before it is coupled into an optical fiber leading to a fiber switch box (*Agiltron, x4 Optical Switch*). This fiber switch box is connected through optical fibers to the cavity fiber and used to switch between the red lasers and the supercontinuum laser. For linewidth measurement (see Fig. 5.2.1), two lasers at $\lambda = 637\,\mathrm{nm}$, namely a *New Focus Velocity TLB-6700* referred

to as the NF laser, and a *Toptica DL pro* referred to as the DLC laser, are used. For measurements at $\lambda = 619\,\text{nm}$, a (*Toptica TA-SHG pro*) laser is utilized. The DLC laser and the 619 nm laser use the same excitation path and are switched as needed by changing the fiber connection. The laser power of the red lasers is regulated by an acousto-optic modulator (AOM). In the 619 nm/DLC path, an electro-optic modulator (EOM) is used for modulating spectral sidebands onto the laser emission frequency. The red lasers are superimposed using a beamsplitter and, again, fiber-coupled to an optical fiber connected to the previously mentioned fiber switch box.

CAVITY CONFIGURATION The optical fiber with the Bragg mirror on its tip is mounted to a manual and piezo controllable z-stage, which allows approaching the plane mirror to form the cavity (see Fig. 5.1.1 d)). The plane mirror is glued using silver conductive paint (*RS PRO Conductive Lacquer*) to a custom-made mirror holder, which is then mounted onto a manual xyz-stage. A round hole in the middle of the holder, above which all platelets on the mirror are placed, allows for the collection of transmitted light from the back of the mirror with an objective. The piezo z-stage at the optical fiber is used for fine control over the distance between the plane mirror and the fiber mirror L_{air}. In contrast, the manual xyz-stage, where the plane mirror is mounted, is used to laterally change the position of the sample with respect to the optical axis of fiber and objective.

MICROSCOPY The transmitted light from the cavity is collected using an objective (*Mitutoyo, Apochromatic x100 Objectives with long working distance*) mounted on a manual stage, allowing for focus adjustment and optical path alignment. Combined with the camera setup, shown in Fig. 5.1.1 c), an optical microscope is formed, allowing for localization of the diamond platelets on the mirror and inspection of the optical fiber tip.

DETECTION PATH Two detection paths, which are selected using a flip mirror, are used for the different experiments performed (see Fig. 5.1.1 b)). In the first configuration, the cavity transmission is collected by an photodiode (PD). The output voltage corresponding to the measured light intensity of the PD is then measured by a computer-controlled oscilloscope (*PicoScope 3403*).

In the second configuration, the light is fiber coupled to an optical fiber which is connected to a spectrometer (*Princeton Instruments, SP-2599i*). The spectrometer is calibrated beforehand using the emission lines of an argon lamp.

5.1.3 CAVITY LENGTH

For all measurements, first, the cavity is formed by approaching the mirror with the fiber tip. Therefore, the manual z-stage is used to coarsely approach, and then by applying a voltage to the piezo z-stage, the cavity is formed ($L_{\text{air,cav}} \lessapprox 15\,\mu\text{m}$). The piezo z-stage is also used to adjust $L_{\text{air,cav}}$.

BARE CAVITY

To measure the length of a bare cavity, a spectrum of the cavity transmission of the supercontinuum laser is acquired. As described by Eqs. (2.3.6) and (2.3.9), only the resonant modes of the cavity are transmitted. The distance between the evenly spaced resonance peaks is defined as the free spectral range (FSR) $f_{n+1}^{\text{res}} - f_n^{\text{res}} = \frac{c}{2 \cdot L_{\text{cav}}}$. Because this expression only

depends on the speed of light c and the cavity length L_{cav}, the latter can be calculated by measuring the FSR. Therefore, a spectrum over multiple resonance peaks is acquired, and the frequency distance between all neighboring resonances is averaged.

HYBRID CAVITY

In a hybrid cavity, the resonant peaks are not evenly spaced, necessitating a different method for measuring the air lengths L_{air} and diamond length L_{dia}. To accomplish this, the piezo voltage of the z-stage is swept, varying L_{air}, and a spectrum is taken at each step. These transmission spectra reveal the resonance frequencies of the cavity for every air length L_{air}, which can be theoretically described for the fundamental modes using Eq. (2.3.13). To convert the voltage axis to a relative length axis, a local conversion factor is first calculated based on the fact that the distance between two neighboring bands at the same frequency corresponds to $\lambda/2$. A cubic polynomial is then fitted to this local conversion factor over voltage data to retrieve the conversion parameters. This accounts for the non-linearity between the piezo voltage and the air length. By fitting Eq. (2.3.13) to the fundamental modes and introducing an additional degree of freedom for an air length offset, $L_{\text{air}} = L_{\text{air}}^{\text{rel}} + L_{\text{air}}^{\text{offset}}$, the absolute cavity length axis and diamond thickness L_{dia} can be determined.

5.1.4 CAVITY LINEWIDTH

To measure the cavity linewidth, the cavity air length L_{air} is swept over a resonant mode of the cavity by adding a sine-shaped voltage to the z-scanner piezo voltage, while the transmission of a red laser is measured on the PD. The measurements are only taken in the approximately linear regime of the sine wave. The cavity linewidth is the full width at half maximum (FWHM) of the transmission peak, which a Lorentzian fit to the data can extract. Because the piezo voltage to cavity length conversion is not directly known, the experiment needs to be extended to extract it from the measured voltage axis of the PD voltage.

For this, two different methods are used in this thesis. For characterization at the resonance frequency of the NV center $\lambda = 637\,\text{nm}$, two detuned lasers (*DLC* and *NF*) with known laser frequencies due to the constant wavemeter measurements, are utilized. Assuming a linear relation between piezo voltage and cavity length, which is reasonable for the small range scanned, the axis can be interpolated from the two known frequencies at the transmission peaks.
At $\lambda = 619\,\text{nm}$, the resonance frequency of the SnV center, only one laser was available. To get the same frequency reference, the laser signal is modulated by the EOM, producing first-order sidebands with frequencies of $f_{\text{mod}} = f_{\text{laser}} \pm \Omega$, where Ω is the modulation frequency applied to the EOM. Because Ω is known, a triple Lorentzian fit to the measured data allows for retrieving the frequency axis as well as the linewidth of the cavity.

5.2 RESULTS

Two different samples were studied in the open microcavity setup, a SnV center-enriched, laser-cut diamond platelet sample (*Vincent Vega*), and a NV center enriched electron beam (e-beam) lithography and dry etching fabricated diamond platelet sample (*Pai Mei*). The cavity linewidth measurements were performed with lasers at the same wavelength as the ZPL wavelength of the color center in the corresponding platelet.

5.2.1 MEASUREMENT PROCEDURE

To characterize the diamond platelets in the open microcavity setup, first, the cavity is formed next to the platelet on the bare mirror. Therefore, a red laser was used, and the air length was scanned using the piezo stage. By applying an offset voltage to the piezo, the air length L_{air} is successively made smaller until resonance peaks of the red laser in the cavity are prominently visible in the oscilloscope connected to the PD. The fiber is moved latterly to optimize on the intensity of the transmission peaks, as this is a good first indication of the amount of additional losses in the cavity. Then a cavity linewidth and a cavity length measurement are acquired to determine the finesse using Eq. (2.3.10). In Fig. 5.2.1 a), a length measurement of the bare cavity, next to a laser-cut, SnV center-enriched platelet (*Vincent Vega*) is shown as an example, while in Fig. 5.2.1 b) the corresponding cavity linewidth measurement is displayed.

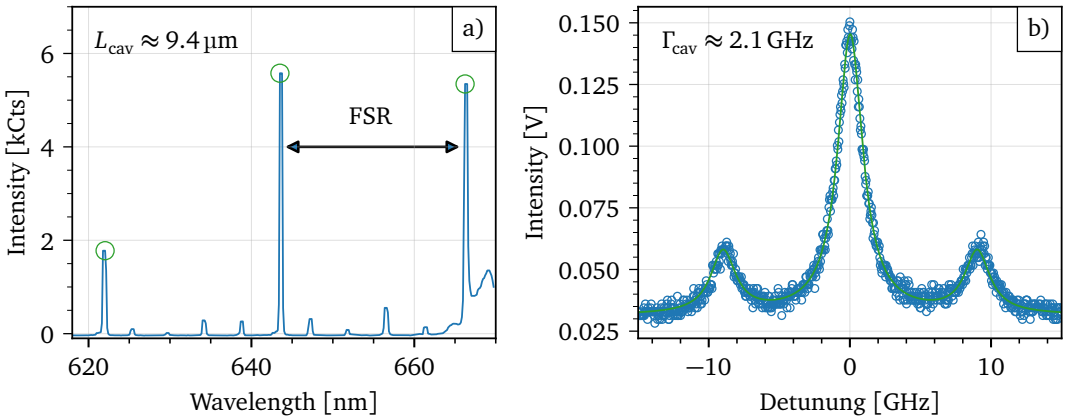

Figure 5.2.1: Measurement results for the characterization of a bare cavity formed next to a laser-cut, SnV center-enriched diamond platelet (*Vincent Vega*). **a)** Cavity transmission over wavelength from a cavity length measurement (*blue line*). The Gaussian first-order cavity resonances are clearly visible as prominent transmission peaks. In addition, less prominent transmission peaks are visible, caused by higher-order Gaussian modes. The transmission peaks are marked (*green circles*), and the average frequency difference between them is measured, which is the FSR of the formed cavity. Using Eq. (2.2.8), the cavity length $L_{\text{cav}} \approx 9.4\,\mu\text{m}$ is obtained. **b)** Frequency over cavity transmission obtained by a cavity linewidth measurement (*blue circles*). A triple Lorentzian is fitted to the data (*green line*). The sidebands modulated onto the laser emission frequency by an EOM are clearly visible. The known detuning of those sidebands of $\Omega = \pm 9\,\text{GHz}$ from the laser emission frequency is used to calculate the frequency axis, as shown in . The linewidth $\Gamma_{\text{cav}} \approx 2.1\,\text{GHz}$ is obtained from the triple Lorentzian fit.

In the next step, the air length is again scanned, while the fiber is latterly moved and positioned over the diamond platelet. Here, the lateral position was optimized on the cavity transmission. Then, a length and a linewidth measurement of the hybrid cavity was performed. In Fig. 5.2.2 a), a length measurement and in Fig. 5.2.2 b), a linewidth measurement performed on the NV center enriched sample is shown as an example. A one-dimensional electric field distribution calculation using the transfer-matrix model was performed to determine the effective length L_{eff} Eq. (2.3.16) of the cavity using the measured air length L_{air} and diamond length L_{dia}. The finesse is then calculated by plugging the measured cavity linewidth Γ_{cav} and the effective length L_{eff} into Eq. (2.3.17). An error of 10 % is estimated for the finesse due to multiple error sources during measurement. For the line-width measurement, a non-linearly behaving piezo can be a source of error. Additionally, as the finesse is calculated using the one-dimensional cavity model, deviates from the real measurement setup are to be expected. The procedure is repeated on multiple spots on the platelet to find a high finesse position. High finesse values could only be retrieved in an air-like mode,

which is expected, among others, since scattering losses at the diamond-air interface are significantly higher in a diamond-like mode [32, 41].

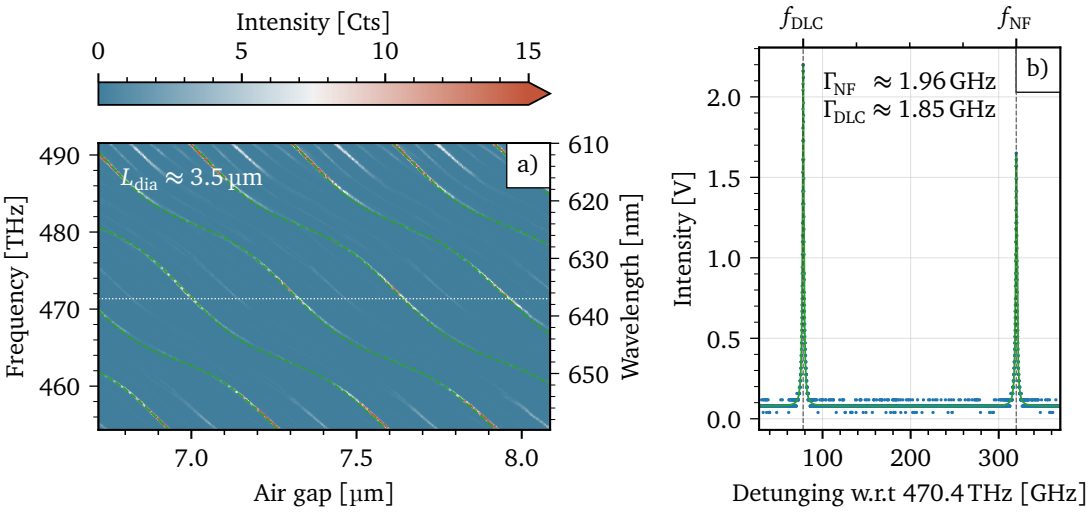

Figure 5.2.2: Measurement results for characterization of a hybrid cavity with a NV center enriched sample, fabricated using e-beam lithography and dry etching (*Pai Mei*). **(a)** Frequency over cavity air gap from hybrid-cavity length measurement. High-intensity lines of the heat map show the resonant modes which are fitted to the theoretical model (*green dashed lines*). Higher order Gaussian modes are also visible [32]. The *white dotted* line indicates the resonant wavelength of the NV center. It is clearly visible that for this diamond thickness, at the ZPL frequency of the NV, the cavity is approximately in an air-like mode. **(b)** Transmission over resonance frequency of the cavity from a cavity linewidth measurement. Both used laser resonances, used to calibrate the x-axis and deduce the cavity linewidth, are clearly visible as peaks in the data (*blue dots*). The fitted double Lorentzian (*green line*), reveals an averaged cavity linewidth of $\Gamma_{cav} \approx 1.9\,GHz$.

5.2.2 ESTIMATION OF LOSSES INTRODUCED BY THE DIAMOND PLATELET

For the NV center-enriched sample (*Pai Mei*), a maximum finesse of $\mathcal{F}_{hc} \approx 3100(300)$ was measured, corresponding to total cavity losses of $\mathcal{L}_{tot,hc} \approx 2000(200)\,ppm$. The highest finesse of a bare cavity formed next to the diamond platelet was measured as $\mathcal{F}_{bc} \approx 12\,000(1000)$, which corresponds to $\mathcal{L}_{tot,bc} \approx 520(50)\,ppm$ losses. After subtracting the losses introduced by the transmission at $\lambda = 637\,nm$ through the plane mirror at $\mathcal{L}_{pm,bc} \approx 280\,ppm$ and the fiber mirror $\mathcal{L}_{fm} \approx 50\,ppm$, additional losses of the bare cavity are retrieved as $\mathcal{L}_{add,bc} \approx 190(50)\,ppm$. These additional losses can be attributed to imperfections in the cavity, for example, scattering losses at the mirror surfaces, a non-perfect spherical shape of the dimple at the fiber tip, or a tilted fiber [32]. Deviations from the specified transmissions stated by *Laseroptik* can also be a factor.

By subtracting all known losses of the hybrid cavity from the measured total losses

$$\mathcal{L}_{add,dia} = \mathcal{L}_{tot,hc} - \mathcal{L}_{pm,hc} - n_{dia} \cdot \mathcal{L}_{fm,hc} - \mathcal{L}_{add,bc}, \tag{5.2.1}$$

an estimation of the losses introduced by the fabricated diamond sample can be made, which was retrieved as $\mathcal{L}_{add,dia} \approx 1200(200)\,ppm$. The reasonable assumption of the cavity being in an air-like mode was made here. No clear reason for the additional losses could be found. The surface roughness of the diamond platelet, with a measured root mean square (RMS) value of $R_q \approx 0.2\,nm$ (see Fig. 3.1.1 b)), should not introduce substantial scattering losses, especially in the measured air-like mode [32]. Other explanations could be absorption in the

diamond, scattering at the mirror-diamond interface, or losses introduced by the mismatch between the plane diamond surface and the curved cavity mode phase [41].

For the SnV center enriched, laser-cut sample (*Vincent Vega*), a similar loss consideration was not possible because there is a mismatch between the specified transmission coefficients and the performed finesse measurement on the bare mirror. With the stated transmission losses, a maximum finesse of $\mathscr{F}_{\text{ideal}} = 6315$ should be achievable. However, a maximum finesse of $\mathscr{F}_{\text{bc}} \approx 8000(800)$ was measured. It was concluded that the mirror reflectivity at $\lambda = 619\,\text{nm}$ is higher than specified by *Laseroptik*. On the diamond platelet a maximum finesse of $\mathscr{F}_{\text{hc}} \approx 2300(200)$ was measured. The lower finesse in comparison to the previously discussed sample is expected due to higher mirror transmission at $\lambda = 619\,\text{nm}$. The additional losses, in comparison to the bare cavity, are $\mathscr{L}_{\text{add,hc}} \approx 1200(300)\,\text{ppm}$, taking the different reflectivity of the mirrors in a hybrid cavity not into account.

5.2.3 ESTIMATION OF THE PURCELL ENHANCEMENT

To estimate an upper limit for the Purcell enhancement of the ZPL of the NV center, the measured finesse is inserted into Eq. (2.2.15). The quantum efficiency is considered to be unity ($\eta \stackrel{!}{=} 1$) [7]. ω_0 is calculated using equation Eq. (2.3.20), with the radius of curvature ROC $\approx 21.8\,\mu\text{m}$ of the fiber dimple and the measured diamond length $L_{\text{dia}} \approx 3.5\,\mu\text{m}$ and air length $L_{\text{air}} \approx 7.7\,\mu\text{m}$. A perfect dipole overlap of the color center with the cavity and positioning of the color center inside the diamond at the maximum of the electric field inside the cavity is assumed for the estimation. Thereby, for the NV center enriched sample (*Pai Mei*) a maximum Purcell factor of $F_{\text{p}}^{\text{ZPL}} \approx 19(2)$ can be expected. According to equation Eq. (2.2.19), this leads to a branching ratio into the cavity mode of $\beta_{\text{cav}} \approx 37(2)\,\%$. This is a substantial increase in ZPL emission in comparison to the intrinsic Debye-Waller factor of $\beta_0 \approx 3\,\%$ [3, 4]. However, in measurements, due to a non-perfect dipole overlap and positioning of the color center with respect to the electric field, a lower Purcell factor is to be expected. In the last step, an estimation of the outcoupling through the bare mirror can be made by comparing the losses through that mirror to the total cavity losses $\beta_{\text{out}} = \beta_{\text{cav}} \cdot \mathscr{L}_{pm,bc}/\mathscr{L}_{\text{tot}} \approx 13(6)\,\%$.

The same estimation of the Purcell enhancement of the ZPL emission was also calculated for the SnV center enriched sample. For the measurements performed on this sample, a different cavity fiber was used with ROC $\approx 20.8\,\mu\text{m}$. The air length is measured as $L_{\text{air}} \approx 6.8\,\mu\text{m}$ and the diamond length as $L_{\text{dia}} \approx 2.3\,\mu\text{m}$. The Purcell factor is calculated to be $F_{\text{p}}^{\text{ZPL}} \approx 15(2)$. The branching ratio $\beta_{\text{cav}} \approx 85(2)\,\%$ is calculated using Eq. (2.2.21). Here, the quantum efficiency $\eta = 0.8$ is considered [2]. As the transmission values of the mirrors are not well known for $\lambda = 619\,\text{nm}$, a reliable estimation of the outcoupling through the plane mirror could not be made. By assuming the losses trough the plane mirror stated by *Lasertec* $\mathscr{L}_{\text{pm,hc}} \approx 1995\,\text{ppm}$, an upper limit of the outcoupling $\beta_{\text{out}} < 62(13)\,\%$ can be calculated.

6 | Conclusion & Outlook

This work aimed to fabricate color center-enriched micro-meter thin diamond platelets and show good optical emitter properties and a high finesse in an open microcavity. For entanglement generation between two color centers, narrow optical lines are important $\Gamma_d < 100\,\mathrm{MHz}$ [7], while for a high Purcell-factor, the additionally introduced cavity Losses by the diamond should be minimal.

Fabrication Multiple diamond platelets bond to several Bragg mirrors could be fabricated by the established method of electron beam (e-beam) lithography and dry etching and by using the novel method utilizing laser cutting. Platelets of both fabrication methods achieved the objective of acquiring a reasonable bonding yield. The most important parameters to achieve this were clean and activated surfaces. For e-beam lithography and dry etching samples, a low surface roughness $R_q \approx 0.2\,\mathrm{nm}$ after applying a strain relief etch could be measured. For the laser-cut samples, tapered and uneven edges are observed, which we attribute to the backside platelet relief etch. The higher surface roughness $R_q \approx 0.9\,\mathrm{nm}$ measured on the laser-cut samples could also be introduced by the backside etch, or it is since too little material was removed during the strain relief etch $d \approx 3\,\mathrm{nm}$.

To reduce the tapering and ruggedness of the edges of the laser-cut platelets, cutting shallower trenches could give an improvement. In addition, implementing a deeper strain relief etch, ideally with interleaved Ar/Cl_2 and O_2 etches, can reduce the surface roughness.

Optical properties Narrow optical lines of nitrogen-vacancy (NV) centers and tin-vacancy (SnV) center emission in platelets could be shown. For the NV center only the spectral diffusion linewidth $\Gamma_s < 80\,\mathrm{MHz}$ could be measured. The narrow linewidth could only be shown in a e-beam lithography and dry etching fabricated sample but could not be reproduced in laser-cut platelets. Further investigation is needed to conclude the reasons for the broadened lines in this sample. For the SnV center, a close to lifetime limited dephasing linewidth $\Gamma_d \approx 32.2(4)\,\mathrm{MHz}$ and a spectral diffusion linewidth of $\Gamma_s \approx 58(2)\,\mathrm{MHz}$ was observed in a laser-cut sample. Both the NV and the SnV center emission linewidths are narrow enough to use the system in future entanglement experiments [7].

Performance in an open microcavity A laser-cut, SnV center-enriched diamond platelet and a e-beam lithography and dry etching fabricated, NV sample enriched diamond platelet was studied in a room temperature open microcavity setup. With the SnV center-enriched sample a maximum finesse of $\mathscr{F} \approx 2300(200)$ at $\lambda = 619\,\mathrm{nm}$, while with the NV center-enriched sample a finesse of $\mathscr{F} \approx 3100(300)$ at $\lambda = 637\,\mathrm{nm}$ could be achieved in an air-like mode. The lower finesse for the first can be attributed to the lower expected reflectivity of the Bragg mirrors at $\lambda = 619\,\mathrm{nm}$. For the latter, by assuming the specified reflectivities of the mirrors, additional losses of $\mathscr{L}_{\mathrm{add,dia}} \approx 1200(200)\,\mathrm{ppm}$ could be attributed to the diamond.

Several factors, such as absorption, scattering losses at both diamond surfaces or losses introduced by the mismatch between the plane diamond surface and the curved cavity mode phase [41] could be an explanation. The maximum achievable Purcell factor and the resulting branching ratio into the cavity mode were estimated using the measured finesse and cavity parameters for both platelet's color centers. For the NV center, a maximum achievable Purcell factor of $F_{\mathrm{P}}^{\mathrm{ZPL}} \approx 19(2)$ and a branching ratio into the cavtiy mode of $\beta_{\mathrm{cav}} \approx 37(2)\,\%$ was calculated. For the SnV center sample, $F_{\mathrm{P}}^{\mathrm{ZPL}} \approx 15(2)$ and $\beta_{\mathrm{cav}} \approx 85(2)\,\%$ where estimated. Both calculations predict a substantial increase in coherent photon emission compared to their behavior outside the cavity. In addition, the outcoupling percentage through the plane mirror was estimated. For the NV center-enriched sample $\beta_{\mathrm{out}} \approx 13(6)\,\%$ was calculated. Comparing this outcoupling percentage of coherent photons to the one achieved by solid immersion lenses $b_{\mathrm{out,sil}} = \beta_0 \cdot \beta_{\mathrm{sil}} \approx 3\,\% \cdot 15\,\% \approx 0.5\,\%$ [46], shows an increase by more than a factor of 20. For the SnV center only an upper limit of $\beta_{\mathrm{out}} \approx 62(13)\,\%$ could be estimated due to the only unreliably known transmission parameter of the mirrors at $\lambda = 619\,\mathrm{nm}$.

In the next step, the Purcell enhancement should be demonstrated in a low-temperature open microcavity by measuring the emitter lifetime while scanning the cavity resonance over the zero-phonon line (ZPL). To utilize the NV center as a quantum network node, another step is achieving microwave control over the spin state. In this thesis, a first experimental step in this direction was done by showing optically detected magnetic resonance (ODMR) with supplied microwaves from gold strip lines deposited on the mirror.

Acknowledgments

First of all, I would like to thank Prof. Jörg Wrachtrup for being my supervisor and for making it possible for me to write this thesis in cooperation with QuTech in Delft. Our meetings always gave me some new insides, especially on the bigger picture of quantum technologies. I also want to thank Prof. Tilman Pfau for being my second supervisor and giving me a good second opinion of my work. Moreover, I want to thank Prof. Ronald Hanson for supervising me and letting me do awesome research in his great group. Not only did you always support me with my physics questions, but you also created an environment where I always felt welcome. Additionally, I want to thank Julia Brevoord and Julius Fischer for being my daily supervisors. Julia, you introduced me to the sometimes exhausting and frustrating world of the cleanroom, but you managed to always make it fun and educative. Thanks for always being supportive, even if your master student sometimes screwed up or lost the orientation in the cleanroom ;). Julius, in addition to introducing me to the cavity lab, you always took a lot of you're time to answer all my questions. Thanks to our discussions, I've gained a new level of insight into color centers in diamond and quantum technologies. Next, I want to thank Yanik Herrmann for his support in the cleanroom and in the cavity lab. Not a lot of people calmly search the floor for 30 min if a master student loses a diamond ;). Additionally, I want to thank Leo Wienhoven for introducing me to the RT-cavity setup and helping me with the analysis of some data from it. I also have to thank Sezer Köse and Elvis van Leeuwen for helping me in the cleanroom and for the valuable discussions regarding fabrication. Thanks to the cleanroom staff of the Kavli Nanolab Delft, especially Roald van der Kolk, Lodi Schriek, Hozanna Miro, Eugen Straver, Charles de Boer, Bas van Asten, and Arnold van Run, for always helping me if my processes didn't work as they should have. I also want to thank all members of Team Diamond for always answering my questions and helping me out. Last but not least, I want to thank my parents Birgit and Sven, my brother Robin and my girlfriend Julia for always supporting me throughout my studies.

BIBLIOGRAPHY

[1] M. Pompili, S. L. N. Hermans, S. Baier, H. K. C. Beukers, P. C. Humphreys, R. N. Schouten, R. F. L. Vermeulen, M. J. Tiggelman, L. d. S. Martins, B. Dirkse, S. Wehner, and R. Hanson, "Realization of a multinode quantum network of remote solid-state qubits", Science **372**, _eprint: https://www.science.org/doi/pdf/10.1126/science.abg1919, 259–264 (2021).

[2] A. E. Rugar, S. Aghaeimeibodi, D. Riedel, C. Dory, H. Lu, P. J. McQuade, Z.-X. Shen, N. A. Melosh, and J. Vučković, "Quantum photonic interface for tin-vacancy centers in diamond", Physical Review X **11**, Publisher: American Physical Society, 031021 (2021).

[3] D. Riedel, I. Söllner, B. J. Shields, S. Starosielec, P. Appel, E. Neu, P. Maletinsky, and R. J. Warburton, "Deterministic enhancement of coherent photon generation from a nitrogen-vacancy center in ultrapure diamond", Physical Review X **7**, Publisher: American Physical Society, 031040 (2017).

[4] A. Faraon, P. E. Barclay, C. Santori, K.-M. C. Fu, and R. G. Beausoleil, "Resonant enhancement of the zero-phonon emission from a colour centre in a diamond cavity", Nature Photonics **5**, Number: 5 Publisher: Nature Publishing Group, 301–305 (2011).

[5] M. Ruf, M. Weaver, S. van Dam, and R. Hanson, "Resonant excitation and purcell enhancement of coherent nitrogen-vacancy centers coupled to a fabry-perot microcavity", Physical Review Applied **15**, Publisher: American Physical Society, 024049 (2021).

[6] S. D. Tchernij, T. Herzig, J. Forneris, J. Küpper, S. Pezzagna, P. Traina, E. Moreva, I. P. Degiovanni, G. Brida, N. Skukan, M. Genovese, M. Jakšić, J. Meijer, and P. Olivero, "Single-photon-emitting optical centers in diamond fabricated upon sn implantation", ACS Photonics **4**, Publisher: American Chemical Society, 2580–2586 (2017).

[7] M. Ruf, "Cavity-enhanced quantum network nodes in diamond", PhD thesis (Delft University of Technology, 2021).

[8] J. Bardeen and W. H. Brattain, "The transistor, a semi-conductor triode", Physical Review **74**, Publisher: American Physical Society, 230–231 (1948).

[9] A. G. J. MacFarlane, J. P. Dowling, and G. J. Milburn, "Quantum technology: the second quantum revolution", Philosophical Transactions of the Royal Society of London. Series A: Mathematical, Physical and Engineering Sciences **361**, Publisher: Royal Society, 1655–1674 (2003).

[10] P. W. Shor, "Polynomial-time algorithms for prime factorization and discrete logarithms on a quantum computer", SIAM Review **41**, Publisher: Society for Industrial and Applied Mathematics, 303–332 (1999).

[11] C. H. Bennett and G. Brassard, "Quantum cryptography: public key distribution and coin tossing", in Proceedings of the ieee international conference on computers, systemes and signal processing, Vol. 560 (Dec. 1984), pp. 175–179.

[12]A. Broadbent, J. Fitzsimons, and E. Kashefi, "Universal blind quantum computation", in 2009 50th annual IEEE symposium on foundations of computer science, ISSN: 0272-5428 (Oct. 2009), pp. 517–526.

[13]P. Kómár, E. M. Kessler, M. Bishof, L. Jiang, A. S. Sørensen, J. Ye, and M. D. Lukin, "A quantum network of clocks", Nature Physics **10**, Number: 8 Publisher: Nature Publishing Group, 582–587 (2014).

[14]S. Wehner, D. Elkouss, and R. Hanson, "Quantum internet: a vision for the road ahead", Science **362**, eaam9288 (2018).

[15]L. Robledo, H. Bernien, I. van Weperen, and R. Hanson, "Control and coherence of the optical transition of single nitrogen vacancy centers in diamond", Physical Review Letters **105**, Publisher: American Physical Society, 177403 (2010).

[16]F. T. Charnock and T. A. Kennedy, "Combined optical and microwave approach for performing quantum spin operations on the nitrogen-vacancy center in diamond", Physical Review B **64**, Publisher: American Physical Society, 041201 (2001).

[17]H. Bernien, B. Hensen, W. Pfaff, G. Koolstra, M. S. Blok, L. Robledo, T. H. Taminiau, M. Markham, D. J. Twitchen, L. Childress, and R. Hanson, "Heralded entanglement between solid-state qubits separated by three metres", Nature **497**, Number: 7447 Publisher: Nature Publishing Group, 86–90 (2013).

[18]M. Ruf, M. IJspeert, S. van Dam, N. de Jong, H. van den Berg, G. Evers, and R. Hanson, "Optically coherent nitrogen-vacancy centers in micrometer-thin etched diamond membranes", Nano Letters **19**, Publisher: American Chemical Society, 3987–3992 (2019).

[19]C. Babin, R. Stöhr, N. Morioka, T. Linkewitz, T. Steidl, R. Wörnle, D. Liu, E. Hesselmeier, V. Vorobyov, A. Denisenko, M. Hentschel, C. Gobert, P. Berwian, G. V. Astakhov, W. Knolle, S. Majety, P. Saha, M. Radulaski, N. T. Son, J. Ul-Hassan, F. Kaiser, and J. Wrachtrup, "Fabrication and nanophotonic waveguide integration of silicon carbide colour centres with preserved spin-optical coherence | nature materials", Nature Materials **21**, 67–73 (2022).

[20]A. Kinos, D. Hunger, R. Kolesov, K. Mølmer, H. de Riedmatten, P. Goldner, A. Tallaire, L. Morvan, P. Berger, S. Welinski, K. Karrai, L. Rippe, S. Kröll, and A. Walther, *Roadmap for rare-earth quantum computing*, Mar. 29, 2021.

[21]H. Bernien, "Control, measurement and entanglement of remote quantum spin registers in diamond", PhD thesis (Delft University of Technology, 2014).

[22]W. Pfaff, "Quantum measurement and entanglement of spin quantum bits in diamond", PhD thesis (Delft University of Technology, 2013).

[23]Y. V. Nazarov and J. Danon, *Advanced quantum mechanics: a practical guide*, Google-Books-ID: BrTP8hEWRGUC (Cambridge University Press, Jan. 3, 2013), 369 pp.

[24]N. Kalb, "Diamond-based quantum networks with multi-qubit nodes", PhD thesis (Delft University of Technology, 2018).

[25]L. Robledo, H. Bernien, T. v. d. Sar, and R. Hanson, "Spin dynamics in the optical cycle of single nitrogen-vacancy centres in diamond", New Journal of Physics **13**, 025013 (2011).

[26]L. Robledo, L. Childress, H. Bernien, B. Hensen, P. F. A. Alkemade, and R. Hanson, "High-fidelity projective read-out of a solid-state spin quantum register", Nature **477**, Number: 7366 Publisher: Nature Publishing Group, 574–578 (2011).

[27]J. Görlitz, D. Herrmann, P. Fuchs, T. Iwasaki, T. Taniguchi, D. Rogalla, D. Hardeman, P.-O. Colard, M. Markham, M. Hatano, and C. Becher, "Coherence of a charge stabilised tin-vacancy spin in diamond", npj Quantum Information **8**, Number: 1 Publisher: Nature Publishing Group, 1–9 (2022).

[28]T. Iwasaki, Y. Miyamoto, T. Taniguchi, P. Siyushev, M. H. Metsch, F. Jelezko, and M. Hatano, "Tin-vacancy quantum emitters in diamond", Physical Review Letters **119**, Publisher: American Physical Society, 253601 (2017).

[29]J. Görlitz, D. Herrmann, G. Thiering, P. Fuchs, M. Gandil, T. Iwasaki, T. Taniguchi, M. Kieschnick, J. Meijer, M. Hatano, A. Gali, and C. Becher, "Spectroscopic investigations of negatively charged tin-vacancy centres in diamond", New Journal of Physics **22**, Publisher: IOP Publishing, 013048 (2020).

[30]Purcell, E.M., "Proceedings of the american physical society", Physical Review **69**, Publisher: American Physical Society, 674–674 (1946).

[31]B. Simons, *Advanced quantum mechanics*, Lecture notes (Department of Physics, University of Cambridge, 2009).

[32]S. van Dam, "Optical cavities, coherent emitters, and protocols for diamond-based quantum networks", PhD thesis (Delft University of Technology, 2019).

[33]M. Fox, *Quantum optics*, 1st ed., Oxford master series in physics (Oxford University Press, Oxford ; New York, 2006).

[34]E. Janitz, M. Ruf, M. Dimock, A. Bourassa, J. Sankey, and L. Childress, "Fabry-perot microcavity for diamond-based photonics", Physical Review A **92**, Publisher: American Physical Society, 043844 (2015).

[35]L. Greuter, S. Starosielec, D. Najer, A. Ludwig, L. Duempelmann, D. Rohner, and R. J. Warburton, "A small mode volume tunable microcavity: development and characterization", Applied Physics Letters **105**, Publisher: American Institute of Physics, 121105 (2014).

[36]D. Hunger, T. Steinmetz, Y. Colombe, C. Deutsch, T. W. Hänsch, and J. Reichel, "A fiber fabry–perot cavity with high finesse", New Journal of Physics **12**, Publisher: IOP Publishing, 065038 (2010).

[37]J. Heupel, M. Pallmann, J. Körber, R. Merz, M. Kopnarski, R. Stöhr, J. P. Reithmaier, D. Hunger, and C. Popov, "Fabrication and characterization of single-crystal diamond membranes for quantum photonics with tunable microcavities", Micromachines **11**, 1080 (2020).

[38]*EL SC plate 2.0x2.0mm, 0.50mm thick*, Element Six, `https://e6cvd.com/us/application/quantum-radiation/el-sc-plate-2-0x2-0x0-5mm.html` (visited on 04/08/2023).

[39]J. Ziegler and J. Biersack, *SRIM - the stopping and range of ions in matter*, SRIM - The Stopping and Range of Ions in Matter, (2013) `http://www.srim.org/` (visited on 04/08/2023).

[40]H. K. Sahoo, L. Ottaviano, Y. Zheng, O. Hansen, and K. Yvind, "Low temperature bonding of heterogeneous materials using al2o3 as an intermediate layer", Journal of Vacuum Science & Technology B **36**, Publisher: American Vacuum Society, 011202 (2018).

[41]J. Körber, M. Pallmann, J. Heupel, R. Stöhr, E. Vasilenko, T. Hümmer, L. Kohler, C. Popov, and D. Hunger, *Scanning cavity microscopy of a single-crystal diamond membrane*, Oct. 11, 2022.

[42]S. Flågan, D. Riedel, A. Javadi, T. Jakubczyk, P. Maletinsky, and R. J. Warburton, "A diamond-confined open microcavity featuring a high quality-factor and a small mode-volume", Journal of Applied Physics **131**, Publisher: American Institute of Physics, 113102 (2022).

[43]W. Pfaff, B. Hensen, H. Bernien, S. B. van Dam, M. S. Blok, T. H. Taminiau, M. J. Tiggelman, R. N. Schouten, M. Markham, D. J. Twitchen, and R. Hanson, "Unconditional quantum teleportation between distant solid-state quantum bits", Science **345**, 532–535 (2014).

[44]K. D. Jahnke, A. Sipahigil, J. M. Binder, M. W. Doherty, M. Metsch, L. J. Rogers, N. B. Manson, M. D. Lukin, and F. Jelezko, "Electron–phonon processes of the silicon-vacancy centre in diamond", New Journal of Physics **17**, Publisher: IOP Publishing, 043011 (2015).

[45]S. Prawer and R. J. Nemanich, "Raman spectroscopy of diamond and doped diamond", Philosophical Transactions of the Royal Society of London. Series A: Mathematical, Physical and Engineering Sciences **362**, Publisher: Royal Society, 2537–2565 (2004).

[46]B. Hensen, H. Bernien, A. E. Dréau, A. Reiserer, N. Kalb, M. S. Blok, J. Ruitenberg, R. F. L. Vermeulen, R. N. Schouten, C. Abellán, W. Amaya, V. Pruneri, M. W. Mitchell, M. Markham, D. J. Twitchen, D. Elkouss, S. Wehner, T. H. Taminiau, and R. Hanson, "Loophole-free bell inequality violation using electron spins separated by 1.3 kilometres", Nature **526**, Number: 7575 Publisher: Nature Publishing Group, 682–686 (2015).

A | FABRICATION METHODOLOGY

In the following chapter, relevant details regarding the fabrication of the diamond platelets are described.

A.1 PLATELET FABRICATION

The fabrication procedures are described in Chapter 3. Here, the parameters and practices are shown.

A.1.1 PECVD OF SiN_x

For deposition of the SiN_x layer, a *Plasmalab 80 Plus* from *Oxford Instruments Plasma Technology* is used. The relevant parameters of the recipe can be found in Table A.1. The diamond membranes are put into the process chamber on top of a 2 cm × 2 cm Si piece.

Parameter	Value
Table temperature	300 °C
Pressure	650 mTorr
SiH_4 flow	20 sccm
NH_3 flow	20 sccm
N_2 flow	980 sccm
low frequency (LF) power	20 W
radio frequency (RF) power	20 W

Table A.1: Recipe parameters for SiN_x plasma-enhanced chemical vapor deposition (PECVD) on a diamond membrane using the *Plasmalab 80 Plus*.

A.1.2 SPIN COATING CSAR-18 AND ELECTRA92

For being able to spin coat and later electron beam (e-beam) expose, the sample is glued onto a 2 cm × 2 cm Si piece using *PMMA 495 A4* (baking: $t = 2$ min, $T = 120$ °C). The *CSAR-18* (*AR-P 6200.13*) is spin coated with 3800 rpm, resulting in a thickness of ≈ 380 nm, and baked at $T = 150$ °C for $t = 3$ min. Afterwards the Electra92 (*AR-PC-5090*) is spin coated on top with 4000 rpm and baked at $T = 90$ °C for $t = 2$ min to avoid charging of the sample during e-beam exposure.

A.1.3 E-BEAM EXPOSURE

For e-beam exposure, an *EBPG5200* from *Raith* is used. The relevant parameters are shown in Table A.2.

Beam Parameters	Value
Acceleration voltage	100 keV
Beam current	267 pA
Aperture	200 µm
Beam step size	2 nm
Resolution	2 nm

Table A.2: Beam parameters for e-beam exposure of the sample using an *EBPG5200*.

A.1.4 DEVELOPING

For development, the sample is first dipped into water to get rid of the Electra92 ($t = 1$ min). Afterward, the sample is developed by first holding the sample in pentyl acetate ($t = 1$ min), then in xylene ($t = 5$ s) and finally in isopropyl alcohol (IPA) ($t = 1$ min) for stopping the process and cleaning. The sample is blow-dried using a N_2 gun.

A.1.5 SiN_x ETCHING

To etch the pattern into the SiN_x layer, an *AMS 100 I-speeder* from *Adixen* is used. The sample is glued on a 4-inch silicon dioxide waver using thermal paste (textitname). The parameters of the recipe used for the CHF_3 etching can be found in Table A.3.

Parameter	Value
Table temperature	20 °C
Pressure	$1 \cdot 10^{-4}$ mbar
CHF_3 flow	60 sccm
O_2 flow	6 sccm
inductively coupled plasma (ICP) power	500 W
RF power	50 W

Table A.3: Recipe parameters for CHF_3 etching the SiN_x layer using the *AMS 100 I-speeder*.

A.1.6 DIAMOND ETCHING

For diamond etching, a *PlasmalabSystems 100* from *Oxford Instruments* is used. The diamond membrane is glued to a 4-inch quartz waver using thermal paste for handling. To transfer the pattern from the hard mask into the diamond, only O_2 etching is used because micro masking in the trenches is not an issue. For the back side platelet release etch, an initial Ar/Cl_2 etch of $t = 45$ min is performed to avoid micro masking. The relevant recipe parameters for the O_2, as well as the Ar/Cl_2 etching, can be found in Tables A.4 and A.5.

Parameter	Value
Table temperature	20 °C
Pressure	10 µbar
O_2 flow	50 sccm
ICP power	1100 W
RF power	90 W

Table A.4: Recipe parameters for O_2 etching of the diamond membrane using the *PlasmalabSystems 100*.

Parameter	Value
Table temperature	30 °C
Pressure	3 µbar
BCl_3 flow	45 sccm
Cl_2 flow	5 sccm
ICP power	600 W
RF power	10 W

Table A.5: Recipe parameters for Ar/Cl_2 etching of the diamond membrane using the *PlasmalabSystems 100* to avoid micro masking.

A.1.7 ORGANIC AND INORGANIC CLEANING

RESIST STRIPPING

To remove the resist *CSAR-18*, the sample is placed in *PRS 3000* for several hours ($t > 12$ h). For two hours of that time, the solution is heated to $T = 80$ °C in a Bain-Marie. Afterward, the sample is rinsed with acetone and IPA before blow-drying with a N_2 gun.

PIRANHA CLEAN

Piranha cleans are carried out for general cleaning purposes. $V = 75$ mL of sulfuric acid (H_2SO_4) is mixed with $V = 25$ mL of hydrogen peroxide (H_2O_2) (Ratio: 3:1) and places into a Bain-Marie at $T = 80$ °C. The sample is placed into the piranha solution for $t \approx 20$ min and afterward rinsed with water, IPA, and N_2 blow-dried.

HYDROFLUORIC ACID (HF) CLEAN

Also, for general cleaning but especially for removing the SiN_x hard mask, hydrofluoric acid (HF) is used. The sample is kept in the acid for $t \approx 15$ min at room temperature and afterward rinsed with IPA and blow dried using a N_2 gun.

CHROMIUM ETCHANT

For etching chromium, the etchant TehniEtch Cr01 is used. The sample is placed into the etchant for $\delta t \approx 15$ min, then rinsed with water, IPA and finally N_2 blow dried.

TRI-ACID CLEAN

The tri-acid clean is performed using

- 20 mL of $HCLO_4$, 60 % *concentration*;
- 20 mL of HNO_3, 65 % *concentration*;
- 20 mL of H_2SO_4.

The acids are mixed in the shown order into the glassware. After the sample is placed into the acids, the temperature is slowly raised until the tri-acid solution starts boiling. The sample is kept in the boiling acid for $\delta t \approx 1\,\mathrm{h}$. Finally, the sample is rinsed with water, IPA, and blow-dried using a N_2 gun.